TAMPEREEN TEKNILLINEN YLIOPISTO
TAMPERE UNIVERSITY OF TECHNOLOGY

ANTON KONTUNEN

A SYSTEM FOR INTRAOPERATIVE CANCER MARGIN DETECTION BY DIATHERMY SMOKE ANALYSIS

Master of Science Thesis

Examiners: Professor Jukka Lekkala and Associate Professor (tenure track) Niku Oksala

The examiners and topic of the thesis were approved on 1 March 2017

ABSTRACT

ANTON KONTUNEN: A System for Intraoperative Cancer Margin Detection by Diathermy Smoke Analysis
Master of Science Thesis, 69 pages
August 2017
Master's Degree Programme in Biomedical Engineering
Major: Biomeasurements and Bioimaging
Examiner: Professor Jukka Lekkala and Associate Professor (tenure track) Niku Oksala

Keywords: cancer margin, diathermy, DMS, FAIMS

Cancer recurrence after surgical operation is a common phenomenon resulting in compromised quality of life, impaired survival and excess costs. Often, the recurrence of cancer is caused by incomplete cancer removal surgery and residual tumor in surgical resection margin due to failure in the cancer margin detection. Currently, the gold standard for the detection is time consuming and expensive analysis of intraoperative tissue specimen by subjective analysis by a pathologist.

In this thesis, a method and system capable of intraoperative cancer margin detection, with potential to improve the current methodology, is introduced, tested and preliminarily validated. The system is based on diathermy smoke analysis by differential ion mobility spectrometry (DMS). Three large measurement sets with different objectives were executed. The first measurement set concentrated on validating the function of a novel filtration device, which is an essential part of the full system proposed in this thesis, and was patented during the thesis work. A study of the composition of different tissue plumes was also done after the filter validation for additional scientific value. In the second measurement set, a proof-of-concept study with porcine tissues was conducted to elucidate, whether healthy tissue identification with the system is possible. The third measurement set was a pilot test with two types of clinical human brain tumor samples, with the aim to achieve actual reliable cancer identification with the proposed system.

Regarding the objectives, all the three measurement sets were successful. Based on the results, we state that the patented filtration solution works with a high efficiency without compromising tissue identification, and that cancer detection based on the ion mobility spectrometer analysis of tissue smoke can be achieved with our system. Although the latencies between possible consecutive measurements do not yet capacitate effective intraoperative identification of cancer tissue, the system can be used to accurately distinguish various healthy tissues and even ultimately differentiate clinical cancer samples.

TIIVISTELMÄ

ANTON KONTUNEN: Diatermiasavun analysointiin perustuva leikkauksenaikainen tervekudosmarginaalin tunnistava mittausjärjestelmä
Diplomityö, 69 sivua
Elokuu 2017
Biotekniikan diplomi-insinöörin tutkinto-ohjelma
Pääaine: Biomittaukset ja -kuvantaminen
Tarkastaja: professori Jukka Lekkala ja apulaisprofessori (tenure track) Niku Oksala

Avainsanat: tervekudosmarginaali, diatermia, DMS, FAIMS

Syövän uusiutuminen kirurgisen hoidon jälkeen on yleinen ja haitallinen potilaan elämänlaatuun ja ennusteeseen vaikuttava ongelma. Se aiheuttaa myös merkittäviä lisäkustannuksia yhteiskunnalle. Usein syövän uusiutuminen aiheutuu syöpäleikkauksen virheellisestä tervekudosmarginaalin arvioinnista, mistä johtuen syöpäkudosta ei saada poistettua kokonaisuudessaan. Nykyinen patologin suorittama toimenpiteen aikana otettuihin kudosnäytteisiin perustuva standardimenetelmä tervekudosmarginaalin tunnistamiseen on hidas, kallis ja subjektiivinen.

Tässä työssä kehitettiin, testattiin ja osittain validoitiin mittausjärjestelmä, jolla tervekudosmarginaalin leikkauksenaikainen tunnistaminen voi olla lähitulevaisuudessa mahdollista jopa leikkaussaliolosuhteissa. Järjestelmä pohjautuu diatermiasavun analysointiin differentiaali-ionimobiliteettispektrometrilla (DMS). Työssä toteutettiin kolme tavoitteiltaan erillistä mittauskokonaisuutta. Ensimmäisessä kokonaisuudessa pyrittiin osoittamaan rakentamamme uudenlaisen suodatinratkaisun toiminta. Työn kanssa samaan aikaan patentoitu suodatinratkaisu on koko järjestelmän toiminnan kannalta välttämätön. Tutkimus eri kudosten savukaasujen koostumuksesta toteutettiin myös ensimmäisessä mittauskokonaisuudessa suodatinmittausten jälkeen. Toisessa mittauskokonaisuudessa tavoitteena oli tutkia, pystytäänkö mittausjärjestelmällä tunnistamaan ja luokittelemaan sian kudoksia. Kolmas mittauskokonaisuus oli pilottimittaussarja, jossa käytettiin ihmisen aivokasvaimia. Tämän sarjan tavoitteena oli nähdä, pystytäänkö järjestelmän avulla luotettavaan kasvaintunnistukseen ja erotteluun.

Tavoitteet saavutettiin kaikissa kolmessa mittauskokonaisuudessa. Tulosten nojalla voimme todeta, että suodatinjärjestelmä toimii tehokkaasti, kudostunnistus on mahdollista ja että diatermiasavun DMS-analyysiin perustuva syöväntunnistus on toteutettavissa mittausjärjestelmällä. Peräkkäisten mittausten väliset viiveet eivät vielä mahdollista tehokasta reaaliaikaista syöväntunnistusta nykyisellä mittausjärjestelmällä, mutta järjestelmällä voidaan kuitenkin jo tunnistaa luotettavasti kudoksia ja jopa erottaa syöpätyyppejä toisistaan.

PREFACE

I could not have hoped for a better or more interesting thesis subject. The research and writing of this thesis has made me realize that I have found a field, where I enjoy working and where I can hopefully also make a notable societal difference. I am extremely grateful to those, who made this thesis research possible.

First, I would like to thank Associate Professor of surgery (tenure track), M.D, Ph.D., DSc(med) Niku Oksala for providing the subject for the thesis, funding the research, for offering his extensive medical expertise throughout the project, and for being an examiner of this thesis. I would also like to thank my second examiner, Professor Jukka Lekkala, who has supported and guided me for the whole duration of my time working in his research group. My heartfelt gratitude goes also to my excellent thesis supervisors M.Sc. Markus Karjalainen and M.D., Ph.D. Antti Roine, who were closely involved in every step of this research and who constantly offered feedback and their guidance during the project. I also want to thank M.Sc. Osmo Anttalainen for offering his help every time, when we had technical problems with our sensor hardware. Lastly, I would like to thank the home front: my family, and especially Kristiina for bearing with me the many long nights of arduous thesis writing.

Tampere, 22.8.2017

CONTENTS

LIST OF FIGURES

LIST OF SYMBOLS AND ABBREVIATIONS

^{241}Am	americium-241
3D	three-dimensional
AC	alternating current
CCR	correct classification rate
CNC	computerized numerical control
DC	direct current
DMS	differential ion mobility spectrometer
DSc(med)	Doctor of Medical Science
ELPI®	electrical low-pressure impactor
eNose	electronic nose
FAIMS	high-field asymmetric waveform ion mobility spectrometry
FN	false negative
FP	false positive
GC	gas chromatography
GC-MS	gas chromatography-mass spectrometry
GUI	graphical user interface
HEPA	high efficiency particulate air
IMS	ion mobility spectrometry
kNN	k-nearest neighbor
LDA	linear discriminant analysis
LOOCV	leave-one-out cross-validation
M.D.	Doctor of Medicine
MS	mass spectrometry
NPV	negative predictive value
OCT	optical coherence tomography
Ph.D.	Doctor of Philosophy
PLA	polylactic acid
PM	particulate matter
PPV	positive predictive value
PTFE	polytetrafluoroethylene
REIMS	rapid evaporative ionization mass spectrometry
RIP	reactant ion peak
TIFF	Tagged Image File Format
TN	true negative
TP	true positive
TUT	Tampere University of Technology
VOC	volatile organic compounds
α	function describing the dependence of mobility on the ratio of electric field to neutral density
η_{filter}	particle filtration efficiency of the electric filter
Δm	mass resolution of a mass spectrometer
E	strength of an electric field
I	electrical current
K	mobility coefficient
K_0	reduced mobility coefficient
M	mass-to-charge ratio

N	number density of gas molecules
N_{ON}	median particle number density of liver tissue measurement when the electric filter is active
N_{OFF}	median particle number density of liver tissue measurement when the electric filter is inactive
P	pressure
Q	heat energy
R	resolving power
T	temperature
t_c	duration of an electrosurgical cut
V	voltage
V_C	compensation voltage
v_d	drift velocity
V_{RF}	voltage of the asymmetric waveform
Z	impedance

1. INTRODUCTION

Cancer is among the leading causes of death in the world, especially in developed countries. According to the most recent global study, every seventh death worldwide in 2012 was caused by cancer, resulting in a total death toll of over 8 million [1]. The annual global incidence of cancer was even higher (over 14 million), but modern cancer treatment has evolved to a point where most cancers can be radiated or surgically operated, which improves the prognosis. Still, in some cases, the treatment or surgery does not prevent the cancer from recurring.

The distance between healthy tissue and excised cancer tissue, also called surgical margin, is critical in terms of the cancer recurrence rate [2,3]. If the margin is too small and all of the cancerous tissue is not removed, it has a negative effect on the prognosis [4]. This is due to increased probability of small clusters of cancerous cells within the margin giving rise to residual cancer tumor and possibly metastasis of the tumor to distant tissues and organs after the operation. On the other hand, if the cancer margin is evaluated deep in to non-cancerous tissue, it results in excessive removal of healthy tissue, which might be harmful for the patient both in terms of physical health (i.e. increased probability of operative complications, physical disability), and mental well-being, and due to needless suffering and changes in physical appearance. In addition, excessive removal of the tissue results in increased duration of the procedure and therefore increased direct costs. The current gold standard for intraoperative cancer margin detection in unclear cases is histological examination of a frozen section obtained during the operation resulting in increased duration of the surgery due to mandatory delay (20–30 min) while waiting for the results [5]. It requires a highly trained professional pathologist, and causes a halt to the already expensive surgical operation, and in the end, the detection is always based on the subjective decision of the pathologist with respect to a point sample from a selected area instead of the whole surgical margin.

Cancer surgery is often performed by utilizing energy-based surgical methods alongside the standard metallic scalpels. One of these methods is diathermy in which the tissue is cut by conducting high-frequency electrical current to the tissue [6]. Depending on the frequency and voltage, the electrosurgical cut may burn the tissue through rapid thermal spreading, effectively creating surgical smoke in the process. The surgical smoke contains 95 % water and 5 % evaporated organic matter from the tissue cells [7]. The gaseous organic matter is composed of blood, organic and inorganic compounds, and micro-organisms [8]. Therefore, it also contains potential biomarkers for cancers, such as various glycerophospholipids [9].

The diagnosis of cancer based on its smell has been done successfully with trained canines [10], but their use in the surgical setting is impossible due to practical reasons. For clinical use, so-called electronic nose (eNose) technology can be considered as a viable alternative. If not using the strictest definition of the term, one example of an eNose can be considered to be a device called a differential ion mobility spectrometer (DMS), which has been successfully used in medical diagnostics to detect gas-phase biomarkers from breath and bodily fluids [11]. Compared to gas chromatography-mass spectrometry (GC-MS), which is widely considered as the gold standard for chemical identification of semi-volatile and volatile organic compounds (VOCs), the benefit of DMS is its simplicity and lower costs. In previous literature, the intraoperative detection of cancer from diathermy smoke has been successfully studied by using mass spectrometry (MS) [9], but similar research with the cheaper, simpler, and more robust DMS technology has not been published.

In this thesis project, the aim was to build, test, improve, and partly validate a system that could potentially be used in intraoperative cancer margin detection by DMS analysis of diathermy smoke. If successful, the creation of such a device could be very significant. It would be an improvement to the relatively slow current standard of pathological examination, and due to its moderate costs ($10 000–$50 000 depending on the manufacturer [12]), it could also be implemented in operating theatres of hospitals in economically developing countries.

The work related to building the system and the measurement sets in this thesis project were done in Tampere University of Technology (TUT), at the department of Automation Science and Engineering (after 1.1.2017, BioMediTech Institute and Faculty of Biomedical Sciences and Engineering). The work also involved co-operation with researchers and medical professionals from University of Tampere. The tumor samples were gathered by the staff at Fimlab laboratories (Tampere, Finland). Parts of the measurement system are commercially available. The main technical novelty of this thesis research is the combination of the newly developed filtration solution (patent pending) together with the rest of the system. All measurements presented in this thesis were done under the guidance of the thesis supervisors, Master of Science (M.Sc.) Markus Karjalainen and Doctor of Medicine (M.D.) Antti Roine.

The thesis consists of six chapters, from which the introduction is the first. The second chapter focuses on the relevant theoretical background. In the third chapter, the measurement system used in the research is thoroughly introduced. The most important measurements done in the thesis project are explained in the fourth chapter. The fifth chapter is dedicated to the results and analysis of the pivotal measurements, and finally, in the sixth chapter, conclusions from all that was done are presented alongside future prospects.

2. THEORETICAL BACKGROUND

The measurement system proposed in this thesis is a prime example of interdisciplinarity. The understanding of the underlying motivation and mechanics behind the system requires knowledge of the medical field, statistical classification, and engineering. This chapter introduces the most important aspects of the relevant theory from each field, with the main focus on engineering. First, a thorough review of the medical background is presented, after which the following four subchapters concentrate on the technical aspects of the theoretical background.

2.1 Medical background

Cancer is the common term for malignant neoplasms (also called malignant tumors), which describe diseases, where proliferation and division of cells is not under control and the cells spread to neighboring tissues via the blood circulation and the lymphatic system, eventually leading to death. Cancers can be classified based on their origin. Brain and spinal cord neoplasms are categorized as central nervous system cancers, leukemia describes cancers that originate from blood-forming tissue, sarcomas start from connective or supportive tissue, lymphomas and myelomas begin growing in the immune system, and carcinomas originate from skin or tissues covering the internal organs. The most common types of cancer are carcinomas in the lung region, breasts (in females), prostate (in males), and liver. [1,13]

Worldwide, over 14 million new cases of cancer are diagnosed annually, accounting for more than 8 million deaths according to the most recently published global study [1]. According to the International Agency for Research on Cancer, the estimated total economic cost of the disease was around 1.16 trillion dollars in 2010 and it is increasing every year [14, p. 576]. Considering these significant global effects of the disease, the motivation for developing new methods to treat, prevent, and diagnose cancer, becomes evident.

Today, cancer can be treated effectively by for example radiation therapy, stem cell transplants, or specialized medication [15]. The surgical excision, i.e. removal of the cancerous tissue is a commonly used treatment method and often used in combination with other approaches such as irradiation, and pharmacological treatment, but in some cases, it can be problematic.

In cancer surgery, full removal of the cancerous tissue is of utmost importance to prevent tumor recurrence which causes additional stress, worsens the prognosis, and increases the costs in the form of follow-up operations [2,3]. To prevent residual cancer tissue

remaining in the patient after surgery, the operating surgeon removes the cancer with a certain appropriate *surgical margin*. This means that along with the malignant tumor, some healthy tissue is removed to ensure a margin free of cancer cells. In an optimal cancer surgery operation, the excision of healthy tissue is kept to a minimum, while still ensuring that all the cancer tissue is fully removed. However, there is not a universal standard or criteria for the values that would constitute a ‘’clear margin’’. Depending on medical center, and the location and type of the cancer, the expert opinions of the measurements vary slightly, but most sources in literature consider 2 mm of normal healthy tissue between the edge and the cancer as the lower limit of a *negative* margin [5,16]. A margin of less than 2 mm is referred to as *close*, and if the cancer is at the edge of the excised tissue piece, the margin is *positive*. If simplified, negative margin would mean that there is high confidence that residual cancer (of that particular cancer mass) is not present after the surgery, while the close and positive margins would indicate the contrary. Illustrations of a negative and a positive surgical margin can be seen in Figure 1.

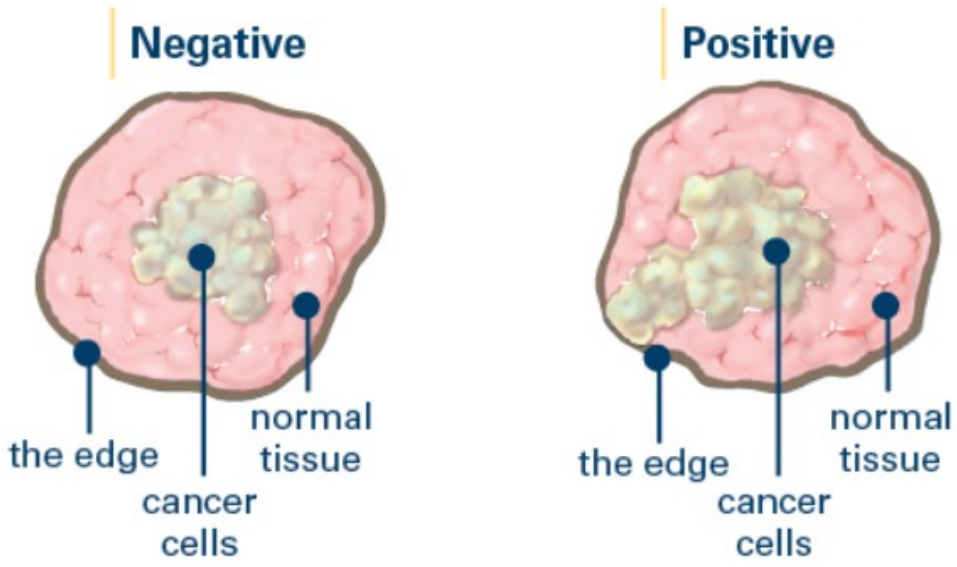

Figure 1. *Illustrations of surgically removed breast cancer samples with a negative and a positive surgical cancer margin.* [17]

The evaluation of the surgical margin is done by a pathologist after the surgery is over, or often in unclear cases also during the operation. The problem with the intraoperative consultation is that it will take 20–30 minutes to finish, when at the same time the patient is waiting anesthezised on operating table [9]. It is also important to note that the evaluation of the margin by tissue samples does not make it possible to analyze all the margin, but it has to be done from selected points of interest. This makes it possible that the margin is not evaluated comprehensively. Neither does it enable to alter the cut line dynamically during the operation. In addition, the use of a qualified pathologist and the prolonged duration of the surgery also increase the total costs of the procedure.

Furthermore, the subjective evaluation of the pathologists is prone to errors. In a retrospective study regarding intraoperative breast cancer margin evaluation, the research showed that almost 20 % of the patients in that study needed additional surgery as a result of false negative margins [18]. The reason why cancers recur due to insufficient surgical margin evaluation and why the resection margin is so difficult to estimate properly is the irregular nature of cancer mass and its tendency to spread in a seemingly random manner. Also, the intraoperative margin assessment is done with a section that has been frozen. This affects the appearance of some tumors, which in turn can lead to erroneous diagnoses [5]. The samples illustrated in Figure 1 can be considered the best-case scenario for the pathologist, since the edges between the tissues are clear and the tumor itself is a uniform entity. In reality, the sections sent to pathological evaluation are often much more difficult to interpret. An example image of a real positive and a close margin can be seen in Figure 2.

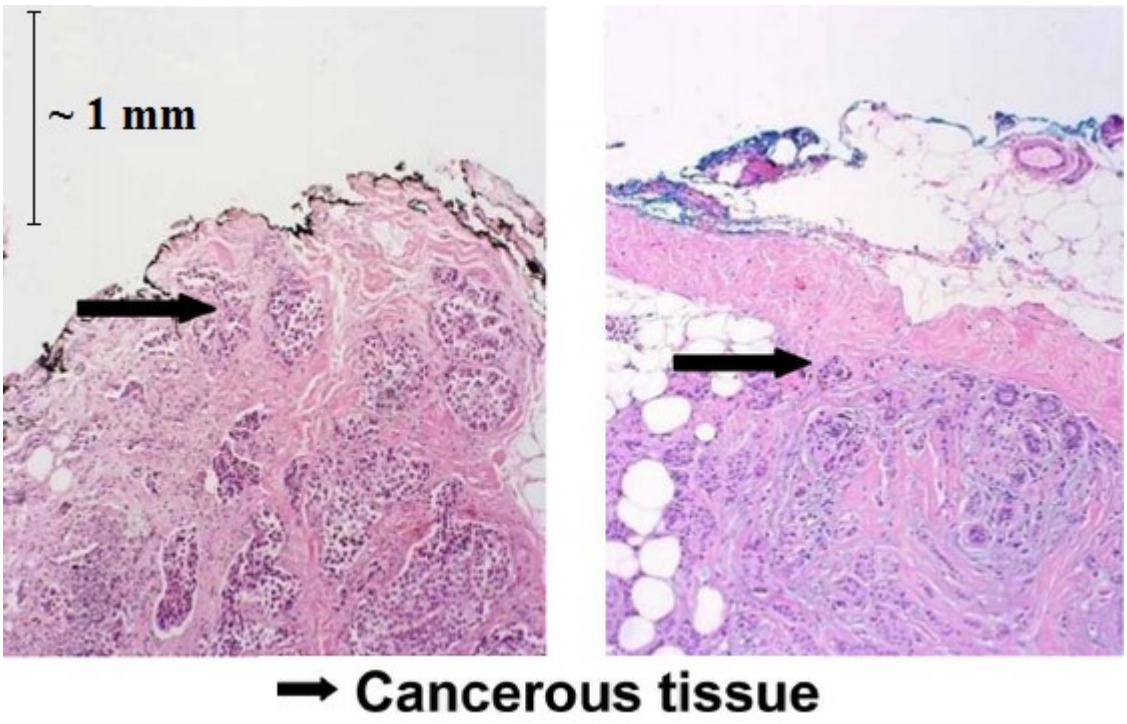

Figure 2. *Photomicrographs of breast cancer sections with positive (left) and close (right) surgical margins. The sections have been stained with hematoxylin and eosin to enable the visual differentiation of the tissue types. Adapted from* [19].

Surgical margin evaluation is especially relevant in the case of breast cancer, since it is the most common cancer type in women, and the recurrence due to false negative margins can be as high as 23 % in some regions [1,20]. To minimize the possibility of errors in cancer margin detection, in some countries operations are often performed by removing the whole cancerous breast (mastectomy). For example, in Finland, mastectomies are performed in 40 % of breast cancer cases [21]. While this lowers the rate of the cancer recurring, the effects of full mastectomy can be harmful for the patient due to

psychological and socioeconomic reasons [22]. Also, breast-conserving surgery can have the same long-term survival rate as a full mastectomy, if it is appropriately used for regional cancers and further treated with radiation [23]. Although every instance is somewhat case-specific, the current global consensus amongst surgeons is that lumpectomies (partial removal of breast) should be preferred over mastectomies [24].

The primary market and area of application for the system proposed in this thesis would be in breast cancer surgery and specifically in the surgical margin detection. However, the system could have use in other areas as well, if the detection accuracy is adequate. Histological examination is always time consuming and requires an expert to make the final diagnosis. A simpler method to find out the malignancy of a cancer sample could save resources, and in this respect the measurements done in this thesis involving the differentiation of two brain cancer types using the system bear real relevance.

The two types of brain tumor samples used in this research were glioblastoma and meningioma. Glioblastoma is the most malignant (grade IV) type of brain tumor that originates from the astrocytes, which are the cells that form the supportive tissue of the brain [25, 26, p. 1306]. The median survival time in glioblastoma cases is only 15 months from diagnosis, and it is also the most common malignant central nervous system neoplasm with an incidence rate of 3.19 cases per 100 000 people in the U.S.A. [27]. When considering all brain tumors, meningioma is the most common type with an incidence rate of approximately 97.5 cases per 100 000 people in the U.S.A., according to a study published in 2010 [28]. Unlike glioblastomas, most cases (95 %) of meningioma are benign [28]. Both cancer types are usually treated surgically, but in the case of glioblastoma a full excision is often impossible due to the cancer being widely spread to the supportive tissue of the brain [29]. With current methodology, the precise information of the cancer type is usually only available after the post-operative histological examination, which means that a reliable intraoperative detection method would be helpful in terms of saving diagnostic resources.

Regardless of the operated tissue type, there is a real need for a system that would improve the accuracy, streamlining or at least complementing the margin evaluation. While there have been efforts to create methods to replace or support the standard of pathological evaluation, none of them have been established as a standard practice. In 2009, a research group introduced a system based on optical coherence tomography (OCT), which reportedly reached 100 % sensitivity and 82 % specificity in intraoperative surgical margin evaluation for breast cancer resections [30]. In OCT, the margin evaluation does not happen *in vivo*, but instead, the surgically removed tumor sample is imaged on a separate platform before the standard pathological evaluation. The OCT scan can provide a high-resolution microscopic image of the tissue piece in real-time, with the maximum imaging depth being approximately 2 mm. The imaging method is based on guiding near-

infrared light to the tissue and measuring the reflected light with a spectrometer. The downsides of OCT are its relatively high unit cost (~$30 000–$50 000 [31]), limited imaging depth, need for subjective analysis by qualified personnel, and sensitivity to surgical artifacts (blood and cauterized tissue) [30,32].

Systems based on intraoperative ultrasound have also been successfully used to evaluate the margins of, for example brain, breast, and renal tumors [33–35]. The method is similar to OCT, but the image is created with high-energy sound waves instead of light. The image is acquired in vivo by inserting a special ultrasound probe inside the patient [36]. Like OCT, intraoperative ultrasound needs visual analysis of the image, and thus it is ultimately a subjective method for the margin evaluation. Also, the unit cost for the more advanced devices can be over $50 000, even when bought used [37].

Regarding the research done in this thesis, perhaps the most interesting and relevant currently existing method that could break through in the field of intraoperative surgical margin detection is rapid evaporative ionization mass spectrometry (REIMS). REIMS is a term first introduced by Schäfer et al. in their publication in 2009 [38]. Since then, the method has been successfully used in identification of different biological tissues and in intraoperative cancer differentiation from healthy tissue, achieving detection accuracies of as high as over 95 % for certain cancer types [9,39]. The operation principle of REIMS relies on thermal evaporation of tissue matter and mass spectrometry (MS) analysis of the resulting gaseous molecules and ions. The distinction between cancerous and healthy tissue is possible by determining the structural differences of evaporated cell contents between healthy and cancerous cells. One major difference between the different cell types is in their phospholipid distributions, which are visible in the MS spectral images [9].

REIMS has already been incorporated into a commercialized device by Waters Corporation (U.S.A.). The "intelligent knife" or iKnife, is a system, where the thermal evaporation of the tissue is done by a standard electrosurgical instrument, after which the tissue plume is guided to a mass spectrometer by using a vacuum pumping system with nitrogen as the carrier gas. The device is capable of analyzing the measured spectrum through multivariate analysis, reaching a diagnosis in approximately 1–3 seconds [9]. Although the device can already be bought by research groups at a price of approximately $700 000 [40], it has not yet (at the time of writing this thesis, August 2017) been made available for clinical use. The high initial cost, and additional costs due to the device being high-maintenance, are factors preventing the system from spreading to wider use. The complexity of the device also means that its operation requires professional training, which hinders the system’s adaptability for surgical staff. In its current form, the iKnife is also too large to fit in an operating theater, without occupying an unreasonable amount of space reserved for vital surgical instrumentation. The more cost-effective, simpler, and

smaller system introduced in this thesis has parallels to the commercialized iKnife, perhaps the most noticeable of which being that both systems rely on the principle of analyzing the chemical composition of the smoke that is created in electrosurgery.

2.2 Diathermy

Electrosurgery, also called diathermy, is one the most common energy-based surgical method used in over 18 million surgeries every year according to some estimates [41, p. 125]. The idea of using electric current in surgical treatment has been around for quite long. For cautering blood vessels, electricity has been used from as early as the 1800s, but the first modern instrument for specifically surgical use, was introduced by William T. Bovie in the 1920s [6].

Diathermy utilizes high-frequency alternating current (AC), which is conducted to the operated tissue to achieve the desired cutting effect [42, p. 15]. When cutting the tissue, a direct contact between the tissue and the surgical electrode is not required, since the current can be conducted via a tissue evaporating electrical arc. The frequency spectrum used in electrosurgery starts at around 200 kHz and extends up to 3.3 MHz [6]. In this frequency range, potentially harmful muscle activations during surgery due to the electrical stimuli do not occur [42, p. 41]. To understand the working principle of electrosurgery, some basic knowledge of electrical engineering is needed. The combined system of the diathermy electrodes and the patient can be considered as a simple closed electrical circuit, where the body of the patient works as a passive component with a certain electrical impedance. In such a circuit, the well-known Ohm's law states that the relation of electrical current and voltage is:

$$I = \frac{V}{Z}, \tag{1}$$

where I is the electrical current, V is the potential difference between the diathermy electrodes (voltage), and Z is the frequency-dependent impedance of the tissue matter between the electrodes. The circuit formed in electrosurgery can be either ground-referenced or isolated. Current will always travel through the path with the least resistance, and in ground-referenced circuits, it can cause problems. If the current density is high upon impact, and the skin contact to the ground potential (usually a grounded plate against the back of the patient) has a small area, there is a risk of inducing an off-site burn on the part of the skin, where the current exits the body. This is the reason, why modern electrosurgical units use isolated generator circuits, where the current always travels through a predetermined route from one electrode to another [6].

From the Ohm's law (1), one can see that the current is inversely proportional to the tissue impedance. This means that the cutting current and the consequential cutting effect are

dependent on the operated tissue and its electrical properties. This is the reason why some modern electrosurgical units can detect the change in tissue impedance and compensate the voltage accordingly to keep the cutting power constant regardless of the tissue [42, p. 27].

The cutting effect of electrosurgical instruments relies on the conversion of electrical energy to heat. The physical phenomenon can be explained with Joule's law of thermodynamics, which can be further formulated to estimate the converted heat energy in a surgical operation as such:

$$Q = I^2 Z t_c, \tag{2}$$

where Q is the heat energy, I is the current, Z is the tissue impedance, and t_c is the duration of the cut. While the thermal energy is an important parameter in diathermy, in itself it does not provide all the information about the characteristics and effects of the surgical cut.

By changing the duty cycle of the current output waveform and the cutting voltage, the thermal spread to the tissue can be controlled, effectively changing the final cutting effect. There are two distinct cutting modes, which have been termed as *pure cut* and *coagulation* (in electrosurgical units often shortened to *cut* and *coag*, respectively). In cut mode, the voltage is low (around 1000 V peak-to-peak) and the current is delivered in a continuous sinusoidal waveform, which has a frequency of around 500 kHz [43, p. 30]. In coagulation mode, the voltage is higher (3000–5000 V peak-to-peak), but the duty cycle of the 500 kHz waveform is low (6 %), which means that the current is not conducted to tissue constantly, but rather as short periodical bursts [43, p. 30]. By choosing the parameters of the current waveform from between the typical cut or coagulation settings, an intermediate cutting mode, called *blend*, can also be used.

In addition to the current waveform, the final effect of the electrosurgical cut is also highly dependent on the density of the current-to-power ratio of the signal conducted to the tissue. This means that the shape and size of the diathermy electrode is an important factor, since the area of the conducting electrode affects how the energy is focused [42, p. 50]. For example, a blade electrode can conduct a much higher current/power density to the tissue if the cut is done by using the edge of the blade instead of the blunt side. In some cases, the phenomenon can be useful, since it would mean that a surgeon could potentially cut and coagulate the tissue just by changing the orientation of the diathermy blade, without changing the diathermy settings.

As the names of the cutting modes suggest, they are used to modify or excise the tissue in different ways. In cut mode, the low-voltage current is conducted to the tissue with high power density, which rapidly increases the temperature of the nearby cells to over

100 °C. The rise of the intracellular temperature causes cellular vaporization, which leads to the release of gaseous organic matter and steam [42, p. 39]. In coagulation mode, the intracellular temperature is meant to rise to over 60 °C, but never above 100 °C, which means that the contents of the cells do not vaporize, but their structure is altered. Instead of instant cell death and cell content vaporization, the effect of coagulation mode electrosurgery is simultaneous cell desiccation (volumetric shrinkage due to cellular dehydration) and protein denaturation, which, when combined, result in a strong tissue seal in the incision area. Due to this phenomenon, coagulation mode is often used to seal blood vessels and other lumen-containing structures [42, p. 46]. The theoretical cutting effect of the blend mode has more variety, since it is dependent on the current waveform properties and how they affect the cell temperatures in the incision area. This means that a more cut-like waveform (high duty cycle, low voltage) is more likely to vaporize the cells and create a surgical incision, whereas a low duty cycle, high-voltage blend will most likely coagulate the tissue. Blend is often used by surgeons to achieve hemostasis while simultaneously cutting the tissue [6, 42 p. 52]. An example of incision patterns created with cut, blend, and coagulation and their associated current waveforms are presented in Figure 3.

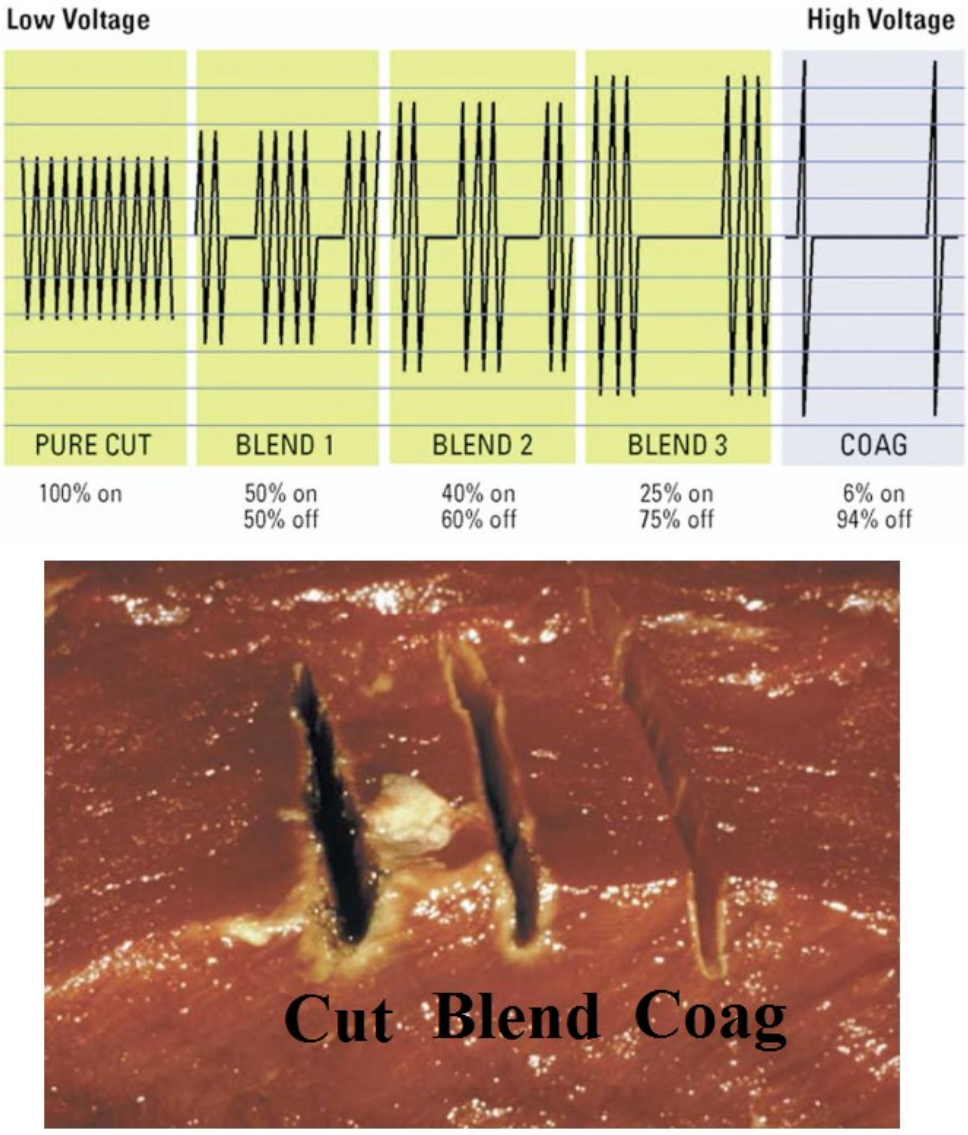

Figure 3. *The current waveforms of different electrosurgical cutting modes (top) and their effect on the produced cutting pattern (bottom). Adapted from* [6].

In addition to cell vaporization and desiccation, a phenomenon called *fulguration* or *black coagulation*, can also happen in electrosurgery. Fulguration is a term used to describe the process, where the intracellular temperature rises above 200 °C, which leads to the organic molecules of the vaporized cells breaking down to their atomic components. When this happens, the resulting carbon atoms create a superficial (approximately 0.5 mm deep) black charred layer in the incision area [42, p. 49]. This so-called carbonization is slightly visible in the incision created with the cut mode in Figure 3.

Like the different cutting modes, electrode shapes and configurations are also used in diathermy to affect the outcome of the surgical incision. The main electrode types are *monopolar*, *bipolar* and *dispersive*. In principle, diathermy is always bipolar, since the current is conducted to the tissue by one electrode, after which it makes its way to the

second receiving electrode. However, in monopolar diathermy, the second electrode is a separate larger dispersive electrode in continuous contact with the patient's skin, whereas in bipolar diathermy, the surgical instrument itself has two active electrodes [42, p. 22]. When using monopolar diathermy, the dispersive electrode should be firmly in place to allow the current to exit the body with low current density, and thus to prevent the off-site burns. An illustration of monopolar and bipolar diathermy configurations can be seen in Figure 4. Both configurations can be used for coagulation and cutting [42, p. 22].

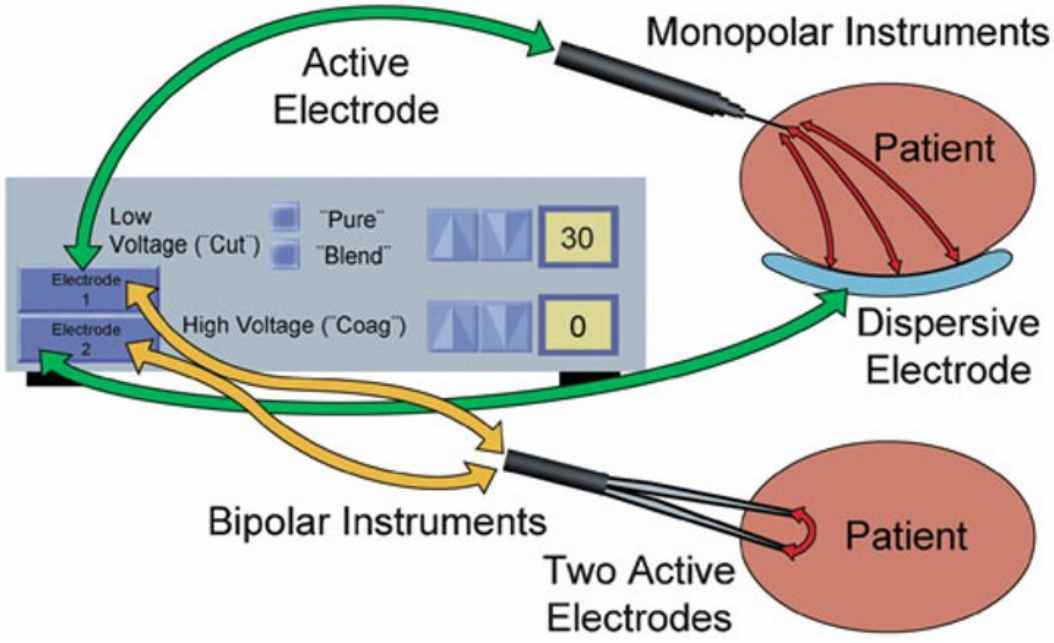

Figure 4. *An illustration depicting monopolar and bipolar diathermy instruments and configurations.* [42, p. 22]

Regardless of the cutting modes or configurations, when diathermy is used in surgical treatment of cancer, some amount of tissue smoke will always be produced as a product of cell vaporization. According to published research, approximately 5 % of the surgical smoke is composed of evaporated organic matter from the tissue cells and the remaining 95 % is water [7]. In addition to the potential biomarkers for cancers, such as phospholipids, the gaseous organic matter in the smoke can contain blood, chemicals, and micro-organisms, including bacteria and viruses [8,44,45]. These findings imply that diathermy smoke is highly hazardous to the operating staff, if the gaseous particles are allowed make their way into their respiratory system. To minimize the exposure to the diathermy smoke, modern surgical instruments have an attached exhaust tube, which can be connected to a surgical smoke evacuator.

2.3 Particle filtration

Not only is the diathermy smoke hazardous to the operating staff through exposure to airborne microbes and particle lung deposition, it can also contaminate the tubes and measurement devices it comes into contact with. That is why, particle filtration is essential in creating a device that is capable of malfunction-free low-latency diathermy smoke analysis.

When considering gas phase substances, particle is a vast term that can be used to refer to any small constituent of matter ranging from gas molecules to the possible macroscopic solid or liquid matter that is suspended in the gas [46]. The combined mixture of the gaseous medium and the liquid or solid particles in it, is called an aerosol, although the term is often misused as a synonym for just the particles in the gas [47, p. 1].

One of the most common methods for particle filtration is the use of fibrous media to separate the continuous phase (gas) from the dispersed phase (solid or liquid) [47, p. 31]. The fibrous filters can be made out of polypropylene, fiberglass, cotton or polyester among other possible materials [48]. The filtration effect of the fibrous filters is based on collecting particulate matter by four individual mechanisms with its substantial number of intertwining fibers [48]. The first method for the filter to collect particles is through *diffusion* in which the particle collides with one of the fibers due to Brownian motion. The second filtration mechanism is called *interception*, which occurs, when the particle is too large to flow through the filter without contact to any of the fibers. *Inertial impaction* is the third mechanism, and it happens, when a particle in a carrier gas flow has too much inertia to bend around the fiber without contact. The particles adhere to the fibers upon impact due to intermolecular forces. The final method for filtration in fibrous filters is *electrostatic attraction*, which is a result of the fiber and the particle having an opposite electrical charge. Electrostatic attraction is dependent on the charge-to-mass ratio, which means that the mechanism becomes more dominant as the particle size decreases. All four mechanisms are illustrated in Figure 5.

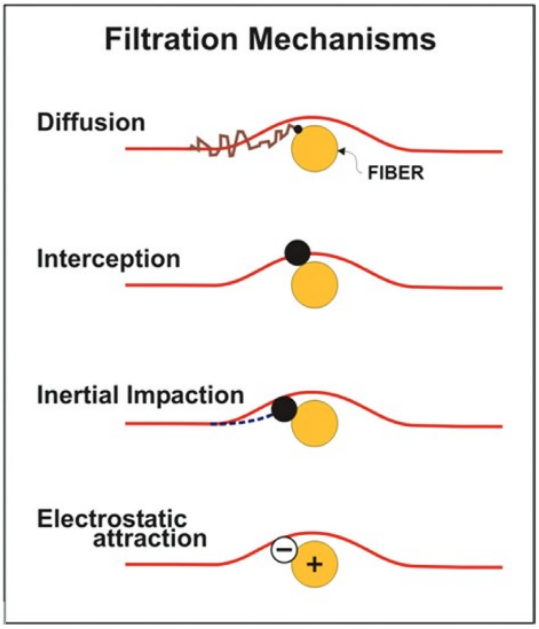

Figure 5. *The four primary filtration mechanisms of fibrous filters.* [48]

Even though the four filtration mechanisms enable the filtration of particles in a wide size range, fibrous filters are not always the optimal method for particle filtration in a low-latency pneumatic system. When considering the measurement dynamics, fibrous filters can be problematic, since they create a pressure difference within the system due to their mesh-like structure [47, p. 49]. In other words, the fiber filters will restrict the natural flow of the carrier gas. To prevent this from happening, a fibrous filter can be replaced with for example, an electric filter, which can remove particulate matter without affecting the sample flow. One possible method for electric particle filtration is particle ionization by a corona discharge, which could be effective in separating the continuous and dispersed phase, if the structure and parameter selection of the filtration device are executed properly. An example of a corona-discharge-based electric filter is presented in chapter 3.

The system proposed in this thesis will be subjected to contaminating aerosols on a daily basis, if it can be successfully developed and implemented in clinical practice. The proper function of the device requires removal of the particulate contaminants, while keeping the gaseous sample intact, and thus providing enough biological information, i.e. gas molecules for the sample to be classified accurately. Therefore, the filtration should be designed with a certain particle size cut-off in mind. When considering electrosurgery, the most probable contaminates to originate from the diathermy smoke are soot particles from unintentional fulguration of tissue, viruses, bacteria, and possible airborne contaminants in the ambient air [8,42,44,45]. These substances are in the size region between 1 nm and 10 µm as can be seen in Figure 6.

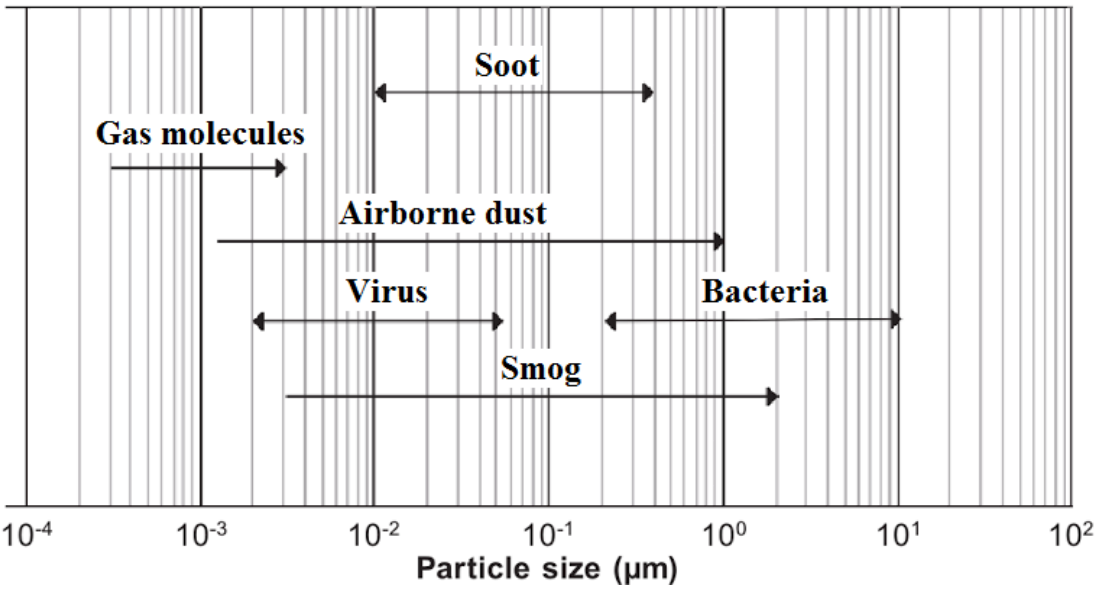

Figure 6. *Particle size range of some substances that are relevant to this research. Adapted from* [47, p. 2].

When considering the system proposed in this thesis, the properties of an electric filter would be favorable. The intraoperative cancer identification requires a system capable of almost instantaneous diagnosis, which means that any large pressure differences, that have a negative effect on the measurement dynamics, should not exist. After filtration, the sample must also retain the distinctive gaseous molecules, which are derived from the cell contents of healthy and cancerous cells. The maximum amount of electric charge of particles is highly dependent on their size [49, p. 301]. Large particles can acquire more electric charge than smaller particles, which means that even with the added inertia of large particles, they can be controlled with an electric field if they are ionized. Based on this, we can assume that filtration in the particle size region of 1 nm to 10 µm is possible to achieve effectively by using a particle-ionizing corona discharge. With a proper design, electric filters can allow the vaporized gaseous molecules and biomarkers from the tissues to pass through, while also keeping the contaminating, larger particulate matter from reaching further.

2.4 Differential ion mobility spectrometry

The fact that the smoke created in electrosurgery contains organic particulate matter and possible biomarkers for cancer would not be helpful without a way to analyze and draw conclusions of its contents. For this purpose, the system introduced in this thesis uses a device called a differential ion mobility spectrometer (DMS), also known as a high-field asymmetric waveform ion mobility spectrometer (FAIMS).

A DMS can be loosely described as a type of an electronic nose (eNose), since it mimics the function of its organic counterpart. Typically however, ion mobility spectrometers are not considered as eNoses in the strictest sense [50], but have been described as such in previous scientific literature [51]. The similarities in the electronic and organic olfaction are important, since the sense of smell has already been utilized in cancer detection by using trained dogs, which has resulted in over 90 % diagnostic sensitivity and specificity in prostate cancer detection from urine samples [10]. Although not yet as successfully as in the case of canine olfaction, the applicability of ion mobility technology in cancer diagnosis has also been tested. In 2014, Roine et al. were able to achieve 78 % sensitivity and 67 % specificity in detecting the malignancy of prostate cancer from urine samples by using a ChemPro® 100i ion mobility spectrometer [52]. The sensor used in the study, much like the most common eNoses, is generally able to detect gas-phase substances in the concentration region of parts-per-million [50, 53, p. 176]. DMS can be considered as a further-developed method of ion mobility spectrometry (IMS), due to its increased detection limit (even parts-per-trillion) and enhanced ion selectivity [54, 53, p. 8].

To understand the DMS technology, a basic understanding of IMS is needed. IMS is a term used to refer to principles, methods, and devices, which characterize substances based on the speed of its gaseous ion swarms within a carrier gas in an electric field [53, p. 1]. In a traditional IMS sensor, an ion swarm from the measured sample is injected into an electric field, where due to its electrical charge, the swarm moves with a certain drift velocity v_d towards a detector. The ionization of the sample can be done by photoionization, corona discharge, or by ionizing radiation by utilizing a radioactive source, among other methods [53, p. 37]. The detector can be for example, a Faraday plate, which generates an electric current signal proportional to the charge released by the ion swarm upon impact. In some DMS devices, there are two detector plates, one for positive ions and one for negative ions [54]. From the drift velocity and the strength of the electric field (E), a mobility coefficient K can be expressed as:

$$K = \frac{v_d}{E} \tag{3}$$

The drift velocity of an ion swarm depends on the internal pressure (P) and temperature (T) of the drift tube, which is why in mobility formulas, K is often normalized to a reduced mobility coefficient (K_0), by using standard conditions, 273 K for temperature and 760 torr for pressure:

$$K_0 = K\frac{273}{T}\frac{P}{760} \tag{4}$$

If the experimental parameters in a measurement are stable, the reduced mobility coefficient is a valid representation of the shape and mass of the ions [53, pp. 1–2].

As its unabbreviated names suggest, the function of the DMS is based on measuring the differences of ion mobility in a high-field asymmetric waveform. In the first publication, where the DMS technology was introduced, the researchers discovered that the trajectory of an ion in a perpendicularly applied electric field changes non-linearly, in relation to the strength of the field [55]. Some ions that have similar trajectories in a low electric field (-1000 V/cm^2) may have totally different trajectories in a high electric field (>20 000 V/cm^2), which enables the differentiation and filtering of the ions, when an asymmetric radiofrequency (>200 kHz) waveform is applied to control the electric field [56]. The electric-field-dependent mobility of the ions in a DMS can be expressed as:

$$K\left(\frac{E}{N}\right) = K_0\left(1 + \alpha\left(\frac{E}{N}\right)\right), \tag{5}$$

where N is the number density of the gas molecules in the sample, and α is a function describing the dependence of mobility on the ratio of electric field to neutral density [53, p. 8]. The physical nature of the ion-specific α is somewhat complex and not yet fully understood. According to a published study, the most prominent hypothesis is that the field-dependence phenomenon can be explained by the sample ion clustering with the drift gas molecules and/or dopant (water or some other VOC) molecules [57]. Depending on α, some ions in the sample chamber will drift towards the electric-field-generating (top and bottom) electrodes due to a phenomenon called direct current (DC) bias shift [56]. This means that without an added DC compensation voltage to the asymmetric voltage waveform, only the ions or ion swarms that are not dependent on E will reach the detector. Ions, which have K_0 on E dependence, will lose their charge before reaching the detector, due to the collision with the top or bottom electrode of the drift chamber. This behavior is illustrated in Figure 7, where a schematic representation of the drift chamber in a DMS device is presented.

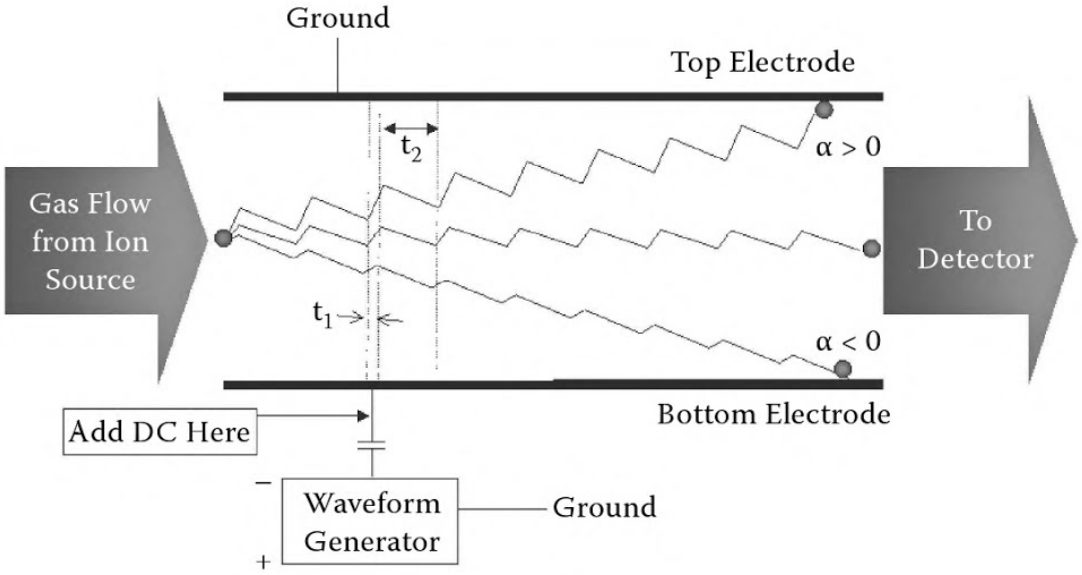

Figure 7. *A schematic representation of the drift chamber in a DMS device. The notations t_1 and t_2 signify the durations of the high-voltage and low-voltage periods of the asymmetrical radio frequency waveform, respectively. α is a function describing the dependence of mobility on the ratio of electric field to neutral density.* [53, p. 9]

The possibility to change the radio-frequency voltage waveform (V_{RF}), and the DC compensation voltage (V_C), enables the high ion selectivity of the DMS. The final output of the device is a data matrix, where every cell (pixel) represents a measured detector response with a certain value of V_{RF} and V_C. The 3-dimensions of the measured data are commonly presented with a two-dimensional color plot, a so-called *dispersion plot*. The y-axis of the plot signifies the values of V_{RF}, and the x-axis shows the values of V_C. The detector response is represented by a color, usually by using a heat map color-scheme, where (in the case of positive ions) the highest value is indicated with red, and the lowest with blue. If the dispersion plot is made for negative ions, the color scheme is reversed. An example of a dispersion plot for a positive ion spectrum measured from the tissue smoke of a porcine brain sample can be seen in Figure 8.

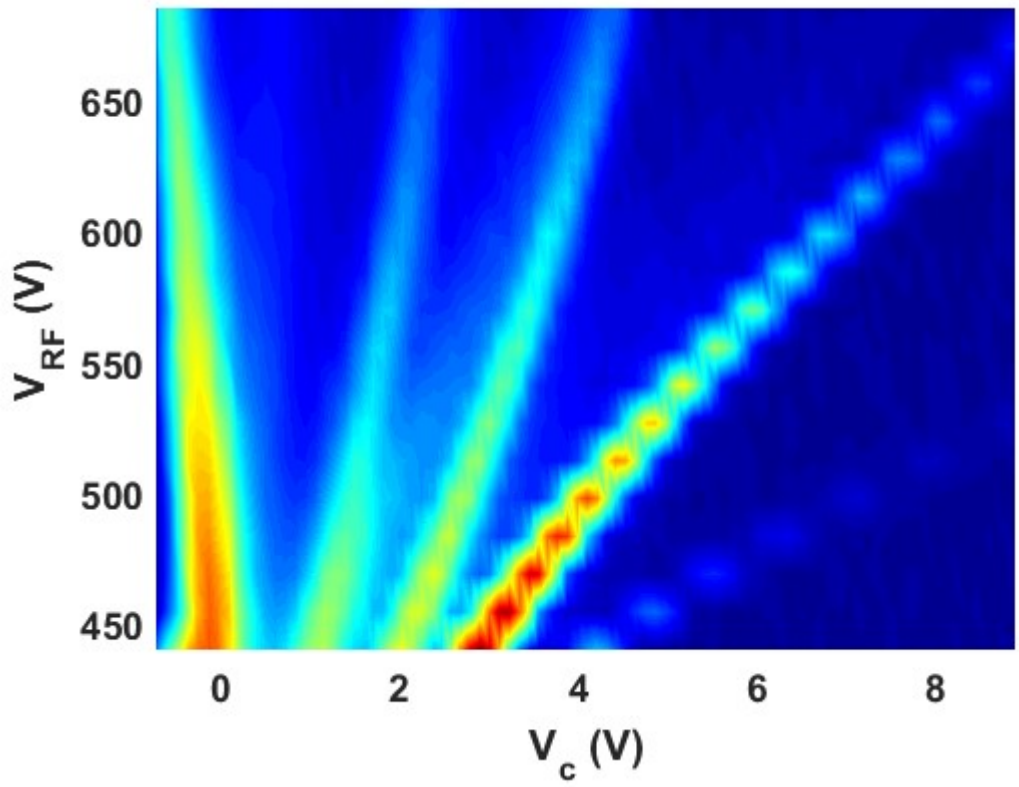

Figure 8. *An example of a dispersion plot for a positive ion spectrum measured from the tissue smoke of a porcine brain sample.*

Perhaps the most important permanent feature in the dispersion plots is the reactant ion peak (RIP), which in Figure 8, can be seen as the rightmost ion ‘’finger’’ (starting from $V_C \approx 3\ V$). The formation of ions from the sample happens mostly through chemical reactions between reactant ions and the sample molecules [53, p. 4]. One example of a reactant ion source is gaseous water molecules in the ambient air. If the RIP is not visible in the dispersion plot, it means that the sample molecules have no reactant ions to react with, to produce sample ions. This means that the measurement can be considered as saturated, which means that distinctive features of the sample might not be visible in the ion spectrum anymore. The saturation of the DMS response can be prevented by lowering the sample concentration. The RIP is a key feature in the dispersion plots, and thus it could be utilized for example in a dilution feed-back loop, which checks the presence or intensity of the RIP with a short (less than a second) sweep, and adjusts the dilution of the sample based on it for the actual measurement.

Even though in some cases the sensitivity of the DMS is a favorable property, it can also become a problem if the concentration between successive measurements varies significantly (from high to low) and if the measurements are conducted in quick succession. When the measurement system does not have enough time to clean itself with purified air or other carrier gas after a measurement, the possible residual molecules

(especially in a high-concentration sample) can affect the dispersion plot of the following measurement due to the high sensitivity of the device.

When considering analytical measurement methods for gas-phase substances, gas chromatography mass spectrometry (GC-MS) is considered as the gold standard, due to its capability for exact quantitative analysis. However, there are some problems in the applicability of GC-MS for certain applications. GC-MS devices measure the sample in a vacuum, whereas DMS works in atmospheric pressure [58]. Also, GC-MS instrumentation is not capable of consecutive low-latency dynamic measurements due to the substance-specific retention times of the gas chromatograph (GC) column, which is needed to separate the compounds before the MS analysis. In addition, the use of GC-MS requires skilled professionals, unlike DMS, which can be operated by anyone, if provided with brief instructions. DMS devices can also be miniaturized, which is an advantage compared to the heavy and space consuming GC-MS instrumentation [58, 53, p. 10]. The cost of the devices is another factor, where the DMS can be considered favorable. Most GC-MS devices are in the price range of $100 000–$500 000 [58,59], whereas DMS devices can be bought with $10 000–$50 000, with the prices depending on the manufacturer [12].

Still, while the GC-MS produces clear information of the components of the measured sample, the analysis of the DMS can be considered as more of a ‘’black box’’ method. This means that the output dispersion plot will not explicitly reveal what kind of molecules there were in the sample, and how many of them were detected. Instead, the output will be a ‘’smell fingerprint’’, which will differ depending on the cell contents of the vaporized sample. However, different molecules can also overlap in the dispersion plot if their mobility is similar enough (and especially if the measurement resolution is limited). When talking about MS, the ability to distinguish the overlapping ion peaks from each other is often described by the term *resolving power* (R), which is dependent on the mass-to-charge ratio of the ions as such:

$$R = \frac{M}{\Delta m}, \tag{6}$$

where M is the mass-to-charge ratio of the ion, and Δm is the resolution in that particular mass-to-charge value [60, p. 25]. This means that the resolving power does not remain constant in the measurement range of the system if the resolution is constant, and vice versa. To clarify with an example, a hypothetical device with a constant R of 3000 will be able to separate an ion with M of 3000 from an ion with M of 3001 (so the resolution is 1). However, the same device could also separate ions with M values of 300.0 and 300.1 (so the resolution in that case would be 0.1). For DMS, the resolving power is defined a bit differently. It is expressed as the compensation voltage at the maximum height of the ion peak divided by the width of the peak at half of its maximum value [53,

p. 172]. When comparing the resolving power, MS is superior to DMS. According to a study, the highest resolving power achieved with DMS is in the region of 400–500, whereas the resolving power of basic MS devices are usually several thousands [61, 60, p. 25]. Despite its few disadvantages compared to (GC-)MS, the advantages of DMS, such as its simplicity, detection limit, price, and capability for fast analysis, makes it potentially more suitable for intraoperative cancer detection from diathermy smoke than other methods.

2.5 Analysis and classification of differential ion mobility spectrometry data

The DMS analysis of two significantly different samples, for example clean air and isopropanol, can produce dispersion plots, which are easy to differentiate even by visual inspection. However, in terms of diathermy smoke generated from various tissues, the differences in the dispersion plots might not be so clear. This is the reason why computational data analysis and machine-learning-based classification methods are needed to achieve a more reliable and effective diagnosis.

In the case of the DMS used in this research, the data stored in a dispersion plot or ‘’smell fingerprint’’ are numerical values that represent the electrical current produced, when the ion (or ion cluster) collides with the detector plate. Each pixel in the dispersion plot is a single current value, which has been measured with a certain V_{RF} and V_C voltage. When analyzing the type of 3-dimensional result matrix that the DMS produces, the amount of data, especially in high-resolution, or consecutive, dynamic, real-time measurements, will expand to a scale that is not feasible to analyze without computational methods.

When the aim of the data analysis is to differentiate multidimensional and potentially dynamic numerical data, the most suitable method depends on the information available. To prevent any possible bias in the analysis of measurement data, scientist in all fields are encouraged to use methods that do not require any preexisting knowledge of the data set (e.g. tissue type) [62]. In the case of machine learning, these methods are referred to as *unsupervised learning* [63]. Unsupervised learning methods aim to find structures in data and learn the decision-making without any examples of what is considered ‘’correct’’. One example of an unsupervised learning method is *hierarchical clustering*, in which an algorithm creates a hierarchical decomposition of the measured data [64]. An example of a machine learning method, which can utilize hierarchical pattern clustering is Self-Organizing Maps also known as Kohonen Maps [65]. In hierarchical clustering, the algorithm does the decomposition by considering each object as an individual cluster, and then begins to search and group similar objects with each other, based on a distance measure that is dependent on the structure of the data. The algorithm can also work the other way around, so that it starts with one combined cluster and then separates them

based on some data features [64]. The output of hierarchical clustering can be visually expressed by a so-called *heatmap*, which presents a data matrix with color-scaled rectangular cells in such a way that the color of each cell corresponds with the numerical value of that element [66]. An alternative presentation method is a *dendrogram*, in which the data are presented in a tree-like structure, where the similar samples are branched together. The clusters that the algorithm considers separate classes, are usually highlighted with distinct colors. An example of a dendrogram can be seen in Figure 9.

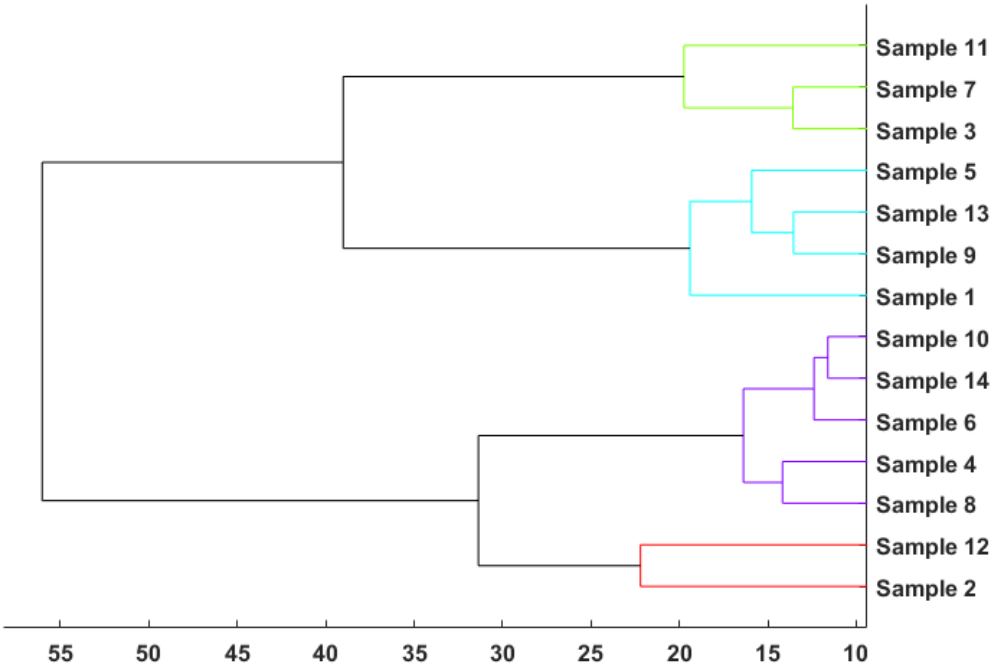

Figure 9. *An example dendrogram made from a measurement set with 14 tissue samples. In this case, the algorithm found four distinct clusters. The x-axis represents an arbitrary distance measure based on the structure of the data.*

If *a priori* information about the real classes of the data set is available, the data analysis and classification can also be done with *supervised learning* methods. The term can be used to describe any machine learning process, where the decision-making process of the algorithm is based on learning data features from a set of known objects (training set) [63]. In the case of classification, the function of the supervised method can then be evaluated with samples in a test set, for which the method has to assign the class. The two supervised learning methods used in this research to classify the tissue samples were *linear discriminant analysis* (LDA) and *k-nearest neighbor* (kNN) classifiers.

LDA is based on Fischer's discriminant, which works by trying to find a projection to a lower dimension for the input variables, while not losing the separability property of the classes [67]. If revised in machine-learning terms, LDA aims to achieve *dimensionality reduction* for the data by *feature projection.* The dimensionality reduction improves the classification accuracy by reducing the variance and noise of the original higher-

dimensional data set [68]. LDA is a common supervised classification method, which has, for example, also been used to classify the results of the REIMS-studies [69].

As the name of the method partly implies, kNN makes the classification decision for a test sample based on what are the k-closest training samples to it in a two-dimensional (Euclidean) plane, with k being a non-zero positive integer [70]. If simplified to the application in this research, this means that the kNN classifier handles the full DMS data set of one measurement as a single point in a two-dimensional plane, and tries to find its closest neighbors in the same dimension-reduced plane. If the k-number of points closest to it are, for example, DMS measurements from liver tissue, the classifier assigns liver as the class of the unknown test sample. In a ''tie'' situation, where e.g. the samples closest to the test sample for 2NN are of different class, the classification is commonly based on which of the training samples is the closest. In other words, ties in kNN classification can be settled with 1NN.

Besides unsupervised or supervised, a machine learning method can also be *semi-supervised*, which means that it combines features from both methods, so that it uses both unlabeled and labeled data [71]. Semi-supervised learning is faster, cheaper, and better than the alternatives in many real-life applications, since the availability of unlabeled data is often far greater than that of labeled data. However, semi-supervised methods can perform worse than supervised learning methods if, for example, the initial parameters or underlying distributions of training data sets have been modelled or assumed wrong [71].

In all machine learning methods, there is a risk of *overfitting*, which means that the training data teaches the algorithm to make its classification decision based on features or values that are not representative of the actual class, but instead are just variance or noise of that particular training set [72]. To increase the reliability of the classifier and to estimate how well the classifier performs with an independent set of data, a process called *cross-validation* is often used [73]. In cross-validation, a distribution of test set and training set pairs are created from a single data set, which makes it an *internal* validation method [74,75]. The alternative way to examine the degree of overfitting in the algorithm is to use *external* validation, in which a fully independent test set from a separate set of data is used. In this research, the classifiers were cross-validated with a method, where the data set is partitioned into as many subsets, as the data set has. The classifier is then tested by using each of the single-item subsets individually as a test set, while every other sample creates the training set [76]. The term used for this method is *leave-one-out cross-validation* (LOOCV).

After a machine learning algorithm has been programmed and validated, there is a possibility to make it adaptive, so that it teaches itself and modifies its decision-making process automatically through new data, without any manual labor by the programmer. In other words, the machine learning task can be implemented in an *artificial neural*

network (ANN), which imitates the biological neural network of the human brain, by basically dividing the task to several layers of neurons [77]. If the ANN has a large number of interconnected hidden layers of these artificial neurons, and a substantial amount of available training data, the process can be described as *deep learning* [78]. In the context of creating a method for intraoperative cancer margin detection, the concept of deep learning becomes relevant, when we reach a point, where the system is already implemented in multiple operating theaters worldwide. If that happens, the data from several thousands of surgeries could be collected in a cloud based data reserve, which would then work as a constantly growing learning basis for the classification algorithm of the system.

Besides the differentiation and classification of multiple sample types, one of the goals of this project is to use the proposed system as an initial method to qualitatively diagnose, whether a certain electrosurgical cut was made to healthy tissue or cancerous tissue. In these kinds of diagnostic tests with a binary outcome, the performance of the method is usually measured with the diagnostic parameters, *sensitivity*, *specificity*, *positive predictive value* (PPV), and *negative predictive value* (NPV) [79]. Sensitivity is used to describe the probability of getting a positive test result, when the test subject has the disease. The value is calculated by dividing the number of true positives (TP) by the total number of the patients with the disease. The probability of not having the disease, when the test result is negative, is described with specificity. Specificity is calculated by dividing the number of true negatives (TN) by the total number of the patients without the disease. PPV is used to express the probability that the patient will have the disease if the test result is positive, and it is defined as the relation of TP to all positive test results. NPV, which is calculated by dividing TP by all negative test results, tells the probability that the patient is disease-free, when the test is negative. Usually the diagnostic parameters of a test are presented alongside a standard 2-by-2 table depicting the number of TP, false positives (FP), TN, and false negatives (FN). An example can be seen in Table 1.

Table 1. *Diagnostic table for a test depicting the values of the most important diagnostic parameters.*

	Disease present	Disease absent	
Positive test result	True positives (TP)	False positives (FP)	$PPV = \frac{TP}{TP+FP}$
Negative test result	False negatives (FN)	True negatives (TN)	$NPV = \frac{TN}{TN+FN}$
	$Sensitivity = \frac{TP}{TP+FN}$	$Specificity = \frac{TN}{TN+FP}$	

Besides the diagnostic parameters, a method or a test needs both high *accuracy* and high *precision*, to be reliable. Accuracy conveys the ability to produce output responses that are true to the expected or real response for the given input, while precision expresses the variability of the output signals (high precision means less variability) [80]. In a DMS for example, high precision and high accuracy would mean that the dispersion plot of a given tissue smoke would be consistently similar in all measurements, and that it would match the actual ion mobility spectrum (the expected ‘’smell fingerprint’’).

Another relevant characteristic of a test, which aims to classify a sample as a certain type, is the overall *correct classification rate* (CCR). CCR is simply the number of the samples that have been classified as the true class, divided by the total number of samples in that class (in this thesis presented as percentage). The complementary term for CCR is *misclassification rate*, which describes the ratio of incorrectly classified samples. If the CCR of the system is high enough in terms of several types of cancers and healthy tissues, the system could be utilized in a more thorough analysis with multiple classes in addition to the simple qualitative ‘’cancer-or-healthy” test. In this kind of a more complex analysis, the classification results from supervised learning methods are often presented in a so-called *confusion matrix*, which is a two-dimensional matrix, where the rows represent the true class of a test sample and the columns represent the class assigned by the classifier [81]. Without the additional statistical parameters calculated from the test results, the diagnostic table presented in Table 1 would also be a special case of a confusion matrix, with only two possible classes. Often, the cells in confusion matrices are colored, similarly as in a heatmap, to help the reader to interpret the results more easily. An example of a confusion matrix, presented in a similar format as the actual results in chapter 5, can be seen in Table 2.

Table 2. *An example of a confusion matrix. The columns represent the assigned class, and the rows represent the actual class for ten samples of A, B, C, and D. In this example, a classifier has misclassified one A sample to class C, and one C sample to class D, while the B and D samples have all been correctly classified. The overall CCR is 95.00 %*

		Assigned class			
		A	**B**	**C**	**D**
True class	**A**	**9**	0	**1**	0
	B	0	**10**	0	0
	C	0	0	**9**	**1**
	D	0	0	0	**10**

3. METHODOLOGY AND MATERIALS

The measurement system used in this research was built in co-operation with doctoral student Markus Karjalainen at TUT. The measurement system can be divided into four distinct parts: the electrosurgical sampling, the electric filter, the differential ion mobility spectrometer, and the computational data analysis. This chapter focuses on each part of the measurement system individually in the aforementioned order. The particle measurement unit used in the first measurement set is also introduced after the main parts of the system.

3.1 Electrosurgical sampling

The first part of the measurement system is the sampling unit, which is used to produce a controlled amount of diathermy smoke accurately and with some degree of automation. The sampling unit consists of a diathermy knife attached to a modified 3D printer, and a smoke evacuator.

The diathermy device is a commercially available Itkacut 350MB (Innokas Medical Oy, Finland), which can be used for bipolar coagulation as well as monopolar coagulation, cutting, and blend [82]. There is no impedance compensation in the device, which means that the voltage remains the same regardless of the operated tissue, which in turn leads to variations in the cutting power between different tissues. Monopolar knife electrodes, which were used in all measurements, were 2.35 mm wide and 0.5 mm thick, and they were manufactured by the company HEBUmedical GmbH (Germany). The movements of the surgical knife electrode were controlled by computerized numerical control (CNC). The CNC device used in the system was built from a REPRAP Mendel Prusa i3 kit (KitPrinter3D, Spain) by Mikael Silenius and Teemu Laine as a part of their bachelor of science thesis research in 2015 [83]. The assembled CNC system is otherwise a normal 3D printer, but the extruder is replaced with a diathermy knife and the heater of the printer bed is disabled, since it serves no purpose in this application. The printer bed is plated with a stainless-steel sheet, which functions as the ground electrode for the monopolar knife electrode. The plate also has an imprinted millimeter grid to help in the sampling process (focusing the knife in relation to the sample piece, and distance estimation). The knife is supported and kept in place at the control frame of the printer by a custom-made polylactic acid (PLA) holder. Next to the surgical knife in the sampling system is an inlet tube made of Tygon®, which is connected to the smoke evacuator. The medical grade smoke evacuator SURTRON® EVAC (LED SpA, Italy) is specifically designed for surgical procedures. The power of the smoke evacuation can be controlled from the front panel of the device, and it can be set to one of the evacuator's predetermined levels 1–9.

When using the lower power levels, the smoke evacuation efficiency of the device during cutting is not always 100 %, so in order to prevent the surgical plume from contaminating the measurement laboratory, all parts of the sampling unit were placed inside a fume hood for the duration of this research. The electrosurgical sampling unit can be seen in Figure 10.

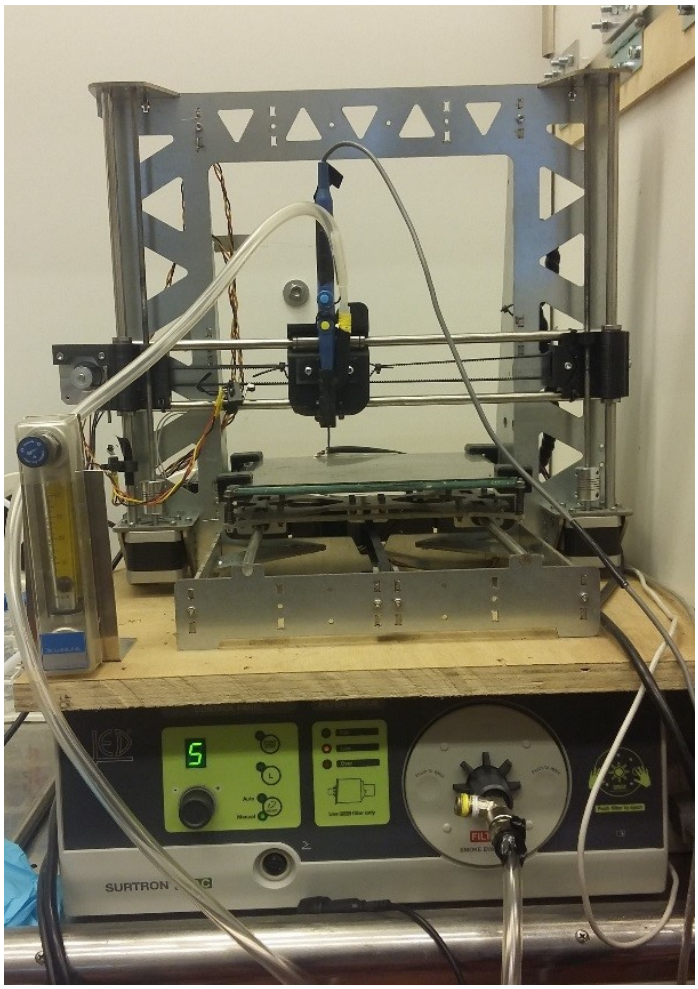

Figure 10. *The electrosurgical sampling unit inside a fume hood.*

The computer control of the surgical instrument in three dimensions is achieved by sending G-code commands to the control circuit of the printer via a serial port connection. G-code, also known as the standard ISO 6983, is the commonly used name of the programming languages utilized in current numerical control systems [84]. The G-code commands were written in MATLAB (The MathWorks Inc., U.S.A) scripts. In addition to assembling the CNC-system itself, Silenius and Laine also created the initial MATLAB-based graphical user interface (GUI), which conveys the script commands to the printer control circuit and which can be used to create an automated measurement sequence with a desired number of electrosurgical cuts. By using the GUI, the user can also determine the cutting pattern, distances between the cuts and depth of the incision.

The possibility to accurately and freely modify the cutting parameters and sequences is essential in creating a standardized research and development model for the measurements, before eventually moving on to clinical practice, where the diathermy knife will be controlled by the operating surgeon. The GUI was created by using MATLAB's GUIDE toolbox. During this thesis project, several changes to the code and structure of the GUI had to be done to accommodate the different measurement protocols and their respective challenges. The graphical user interface in its final form after the brain tumor measurements is presented in Figure 11.

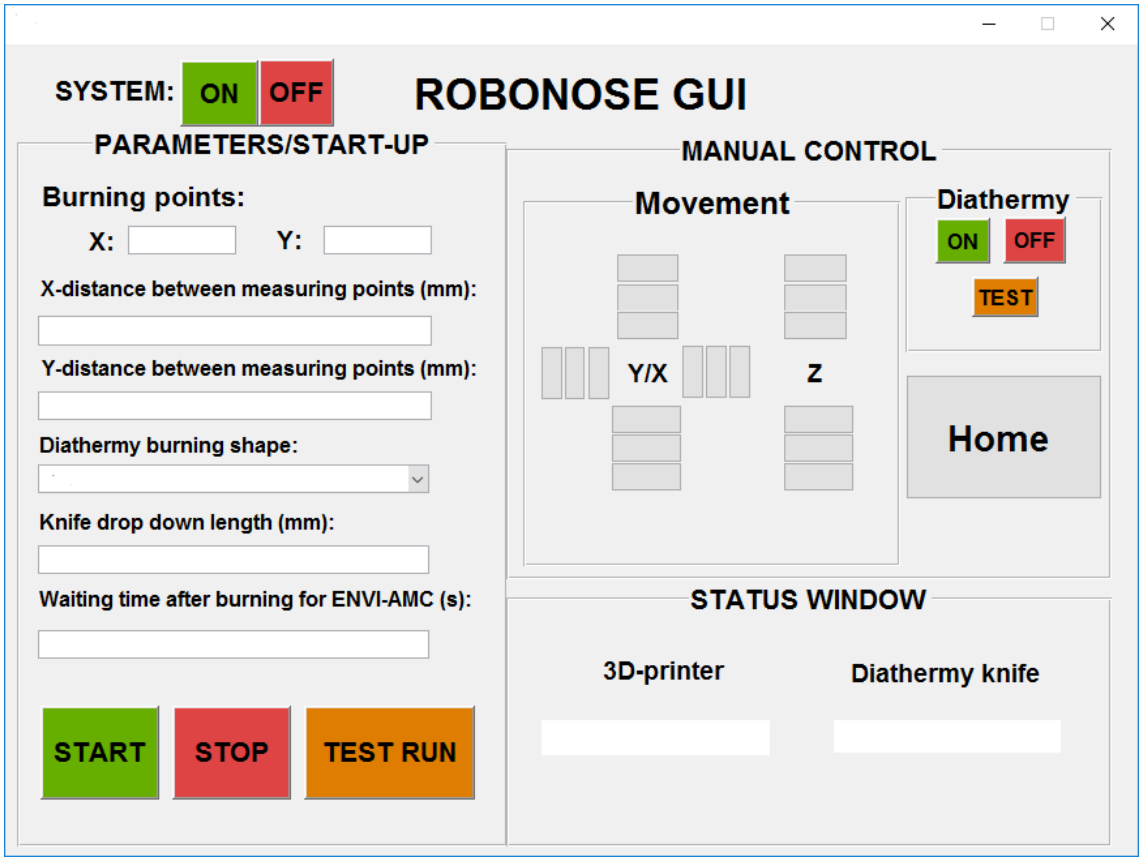

Figure 11. *The graphical user interface of the CNC sampling unit. The communication port connection between a computer and the CNC device can be established and disabled by the push buttons on the upper left corner. The PARAMETERS/START-UP block can be used to create an automatic measurement sequence with the desired cutting parameters. The sequence can be executed, stopped, and tested (without activating the diathermy knife) by the push buttons on the bottom. The MANUAL CONTROL block can be used to manually alter the state of the diathermy knife and move it in three dimensions. The Home button moves the knife to the starting position (X = 0, Y = 0, and Z = 0). The STATUS WINDOW block shows the status (ON/OFF) of the CNC-computer connection and the diathermy knife.*

3.2 The electric particle filter

The plume created by the diathermy knife in electrosurgical operations is rich with different-sized particulate matter, which is not only dangerous to the operating staff, but which will contaminate the measurement system if left unaltered. That is why, directly after the electrosurgical sampling unit, the electric particle filter is the next active component in the measurement system. The inlet tube of the filter is connected to the smoke evacuator inlet by a brass T-connector. Part of the produced surgical plume will go through the electric particle filter instead of reaching the smoke evacuator, since there are M/58112/09 (Norgen Finland Oy, Finland) vacuum ejectors on the outlet ports of the electric filter, which create a negative pressure and thus guide part of the sample flow towards the filter inlet. The electric particle filter, its schematics, and the combination of the filtration solution with the rest of the proposed system are intellectual property owned by the Finnish company Olfactomics Ltd (Patent number: 20175319, patent pending) [85].

The structure of the filter is relatively simple. It consists of a 1 mm thick cylindrical copper casing with an inner diameter of 20 mm, PLA end pieces that hold the casing in place, and a corona needle made from stainless steel. The filter has one inlet and two outlet ports. The inlet and outlet connectors are made from stainless steel. The first outlet in the outer rim of the second PLA end piece is designed to work as a waste outlet for the filter by removing large particulate matter. The second outlet port is located at the stem of the corona needle. A 3D schematic representation of the electric filter with its key structural points highlighted can be seen in Figure 12.

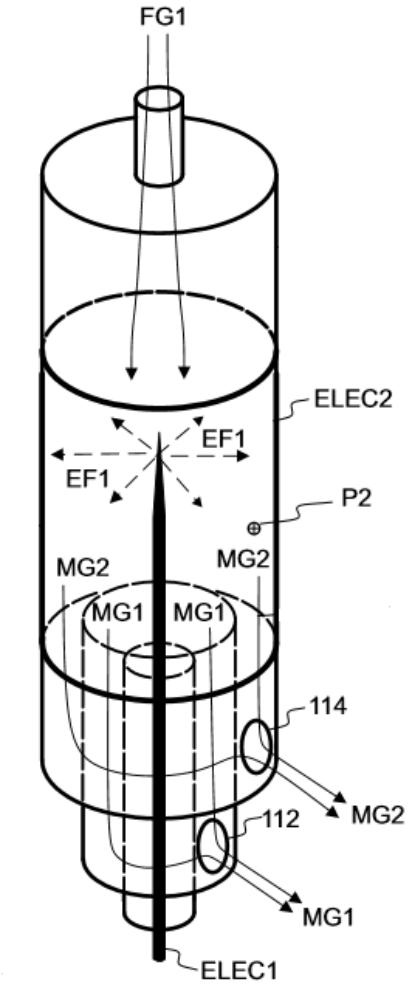

Figure 12. *A 3-dimensional schematic representation of the electric filter. The abbreviations refer to the structural key points of the filter: FG1 is the unaltered inlet flow, EF1 is the electric field created by the potential difference between the corona needle (ELEC1) and the cylindrical copper casing (ELEC2), P2 is a positively charged particle created by the corona discharge, MG1 is the sample flow with only the neutral gas phase molecules egressed by the sample outlet (112), and MG2 is the waste flow, which exits through the waste outlet (114). Adapted from* [85].

The function of the filter relies on creating a corona discharge, which ionizes the incoming large smoke particles (µm-range and higher particle diameter), but leaves the small gas phase molecules (pm or nm-range particle diameter) neutral. In these measurements, we created a positive corona discharge by using a SL50P10 high voltage source (Spellman High Voltage Electronics Corporation, U.S.A.). The maximum value for the potential of the corona needle was designed to be 5 kV, due to the voltage limit of the safe high voltage connectors between the voltage source and the filter. When the larger particles are charged, they drift towards the copper casing of the filter due to the electric field created by the potential difference between the needle and the casing. Upon impact, the particles lose their electric charge, and adhere to the filter casing. Depending on the total airflow going through the filter, some of these particles might detach from the casing and return

to the airflow. These particles will not however contaminate the sample flow, since they will drift towards the waste outlet on the outer rim of the filter. By keeping the measured sample flow free of large contaminants, the electric particle filter enables multiple consecutive measurements and thus is essential in creating a functional device that could withstand hours of surgery without contamination-related malfunctions. In addition, the design of the filter is especially favorable in terms of measurement dynamics. Unlike, for example, glass fiber filters, the electric filter does not hinder the flow of air at any point, and thus does not significantly affect the kinetics of the measurement. This is an extremely crucial property when considering the ultimate real-time target application of this research.

Another potentially favorable property of the electric filter is that it produces ozone as a result of ionizing the oxygen molecules in the carrier gas (if the carrier gas contains oxygen) [86]. Ozone is a powerful oxidant, which can eradicate viruses and bacteria by destroying the cell walls of the micro-organisms by an oxidative burst [87]. This means that the harmful micro-organic contaminants in the diathermy smoke will not only be filtered by the electric filter, but also potentially inactivated, preventing any bacterial growth within the exhaust tubes or the filter casing. In a brief separate measurement done after the thesis research, the ozone creation in the electric filter was studied by using Model 205 Dual Beam Ozone Monitor™ (2B Technologies Inc, U.S.A). The measurement revealed that with similar parameters as used in the thesis research, the filter is capable of producing an estimated 0.5–2.0 ppm concentrations of ozone, depending on the corona discharge current and total air flow through the filter. In water, these concentrations are enough to destroy over 99 % of common bacteria and viruses in seconds, but in air, the same percentages require a longer exposure time (minutes) or higher ozone concentrations (hundreds of ppm) [88]. The ozone production in the filter could be increased with some technical modifications, for example, by making the corona needle from a different metal, or by creating the corona discharge with negative voltage instead of positive [89].

3.3 ENVI-AMC® differential ion mobility spectrometer

After the preliminary sample has been modified by the particle filter to remove the soot particles and other contaminants, the mobility of the remaining molecules can be measured. The measurement is conducted with an ENVI-AMC® differential ion mobility spectrometer. The DMS device was manufactured by the Finnish company Environics Oy and it was primarily designed for real-time ultra-low level detection of ammonia and acids in clean room facilities [90]. The device uses an americium-241 (^{241}Am) radioactive isotope as its ionization method, and according to its technical datasheet it can detect substances in the concentration region of parts-per-trillion (ppt) in seconds [90]. The output quantity of the device is a pA-scale electric current, which is produced, when the

sample ions reach the detector plate and lose their electric charge. The favorable properties of the device, such as its sensitivity, price, and available technical support (courtesy of M.Sc. Osmo Anttalainen) were the reasons why the ENVI-AMC® was chosen as the primary measurement device. The possibility to freely modify the measurement scripts to match different purposes was also extremely suitable for this research and the development of the system, since it allowed iterative experimentation and determination of optimized analysis parameters.

Even though the electric particle filter removes the large particles, the over-abundance of small gas-phase scent molecules in the sample flow is still too much for the sensitive ion mobility spectrometer to measure without becoming saturated. That is why, before the sensor, the sample flow was diluted in all measurements by a two-fold dilution system. The dilution was done by feeding the sample gas to M/58112/09 vacuum pump ejectors with dilution gas coming from TUT's central pressurized air pipelines. Before the ejectors, the pressurized air passed through a cylindrical steel container filled with 0.5 nm molecular sieves, and a second container filled with active carbon, to make sure that the carrier gas was dry and free of contaminants. The dilution system was connected to the electric filter sample outlet and ENVI-AMC® by polytetrafluoroethylene (PTFE) tubing.

Like every other commercially available DMS device, the function of the ENVI-AMC® is based on creating strong electric fields and differentiating the ion clusters by an asymmetric periodic electrical waveform. Almost all of the measurement parameters can be altered, and different measurement protocols with varying duration and resolution can be made by creating scripts in the device's own GUI. The GUI can be accessed by connecting a monitor to the device or by using an internet browser in a shared wireless network. The scripts are written in the scripting language Lua, which is an embeddable, lightweight, and fast language commonly used in many industrial applications and video game programming [91, p. 2]. When using a basic script, where the compensation voltage (V_C) and the voltage of the asymmetric waveform (V_{RF}) rise in regular increments, a dispersion plot of the ion mobility spectrum is shown on the main page of the GUI after a measurement. An example of this type of a typical dispersion plot created by the ENVI-AMC®, when measuring purified pressurized air can be seen in Figure 13. In addition to the ion spectrum, the device also saves useful metadata, such as ambient temperature and humidity values of the measurements in its memory, from where they can be downloaded for further processing and analysis.

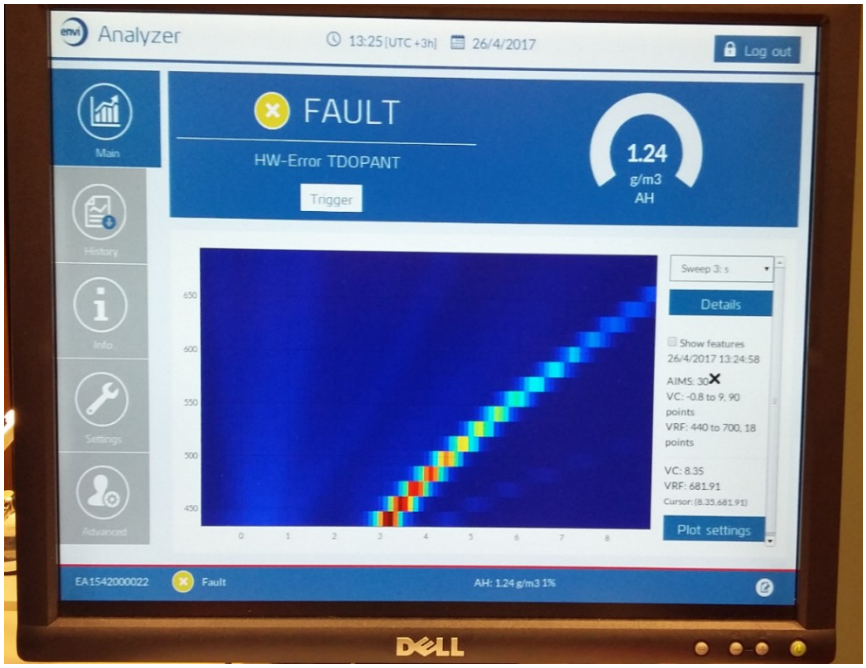

Figure 13. *An example of a dispersion plot from dried and filtered air as seen in the ENVI-AMC® graphical user interface. Without an actual sample, the only distinctive feature in the dispersion plot is the RIP.*

3.4 Data analysis

The ENVI-AMC® GUI can be used for simple qualitative visual inspection of the data to detect, for example, a notable change in the level of ammonia in a clean room, but in more complicated measurements, computational data analysis is needed. In this research, the chosen method for the analysis was MATLAB-based processing and classification algorithms. Due to the complex multidimensional nature of the DMS data and changes in the measurement protocols, multiple scripts had to be made. Even though the measurement data was not the same type in all the measurements, the analysis in almost all cases can be divided into four phases: initial download of the raw data from the measurement device to a computer, pre-processing and modification of the raw data, calculations or classification based on the modified data, and graphical or numerical representation of the analysis.

The data from the first measurement set was largely different from the other two sets, since the measurements were not done with the ENVI-AMC®, but instead, only the filtration efficiency of the electric filter was studied by measuring mass changes, color intensities, and particle distributions. The analysis based on mass changes was done by simply comparing the measured mass values, which were acquired with an XR 205SM-DR semi-micro balance (Precisa Gravimetrics AG, Switzerland, readability 0.01 mg). The processing of the particle distribution data was also straightforward, since the analysis only required modification of the raw data from the used electrical low-pressure

impactor with a pre-made MATLAB-script. The color analysis of the filtration efficiency was done by using the sum of the pixel color intensity values from a 16-bit color-coded planar scan of glass fiber filters as a metric for the contamination level in cases, where the electric filter was either active or inactive. In a 16-bit color-coded image, each pixel is represented by a vector with three elements. These elements represent the intensity of the colors red, green, and blue in the pixel and their numeric value is an integer between 0 and 65535 (2^{16}-1). In order to simplify the contamination metric to just one numeric value, the individual scans of the filters were first transformed to grayscale images. This means that each pixel of the modified images had only one of the 65536 different shades of gray and thus, the color intensity of each pixel could be represented by only one value instead of three. The intensity range of the grayscale image pixel value was normalized and reversed, so that value 0 equaled the brightest shade (white) and 1 equaled the darkest (black). A metal casing in which the glass fiber filters were placed during the measurement, prevented the full contamination of the glass fiber filters, which meant that a large area of the filters was not affected by the smoke at all and consequently was not dyed by the surgical smoke. Therefore, the color analysis was done to an area of 200×200 pixels from the middle of each filter, even though the resolution of the initial scans with the used Epson Perfection 4870 Photo scanner (Seiko Epson Corporation, Japan) was 9600×9600.

As for the measurements based on DMS responses, the steps in the data analysis were more similar in all measurement sets. First, the raw data of all measurements in the set were downloaded from the ENVI-AMC® to a computer. The raw data were then pre-processed to remove possible unwanted measurements, to add descriptive data (tissue type), and to slightly modify the structure of the data. After the data were pre-processed, the actual classification was done. The supervised classification methods that were used, were LDA and kNN. Both classifiers were programmed by using the pre-existing MATLAB functions (fitcdiscr for LDA, and fitcknn for kNN). The classifiers were cross-validated by using LOOCV. After the creation of the cross-validated classifier, the pre-processed data matrix was analyzed and the classification results were presented in a confusion matrix. The initial pre-processing, and classification scripts were made by D.Sc. Pekka Kumpulainen and medical student, B.Sc. Lauri Hokkinen. During the thesis research, several changes to the initial scripts had to be made to accommodate the changes in measurement parameters.

By combining the electrosurgical sampling, the electric particle filtration, ENVI-AMC®, and the data analysis, the framework for a system capable of diathermy smoke analysis is complete. Still, the modular nature of the system enables some experimentation and modification to the ensemble, without needing to fully disassemble the complete device.

3.5 Electrical low-pressure impactor

In addition to the four main modules of the measurement system, an electrical low-pressure impactor (ELPI®, Dekati Inc., Finland) was needed in this research to validate the function of the electric particle filter. The ELPI® system was also used for the additional particle mass, size, and number distribution measurements, from which the results are presented in a separate journal article, which was submitted for publication during the thesis work [92]. The ELPI® system used in the measurements was loaned from the department of aerosol physics at TUT. The ELPI® replaced the DMS as the primary measurement device for the diathermy smoke in the first measurement set.

The ELPI® system is capable of real-time particle size, mass, and number distribution measurements for particles in the size range of 7 nm to 10 µm [93]. The function of the system can be divided into three parts. First the particles in the measured aerosol sample are charged with a unipolar corona charger. Then, the charged particles enter the impactor region, where a cascade low-pressure impactor collects the different-sized particles with insulated collection plates. Lastly, the charge of the incoming particles is measured in real-time by sensitive electrometers. The resulting current signal is directly proportional to the size, and number concentration of the particles, which means that from the real-time current value, the particle concentration and size distributions can be derived [94].

4. MEASUREMENTS

The aim of this research was to test the capability and functionality of the proposed measurement system, first in tissue identification and finally in cancer detection. Before the actual tissue measurements, the functionality of the electric particle filter was verified by particle measurements. In this chapter, the goals, measurement protocols, and the used equipment for each measurement are specified. All the measurements in this research were conducted in TUT at the department of Automation Science and Engineering (after 1.1.2017, BioMediTech Institute and Faculty of Biomedical Sciences and Engineering). The flow rates were measured and calibrated with Gilian Gilibrator-2 NIOSH Primary Standard Air Flow Calibrator (Sensidyne, Schauenburg International GmbH, Germany). All non-human tissue samples used in the measurements were acquired from a slaughterhouse (Paijan Tilateurastamo, Urjala, Finland) or from a normal grocery shop. The human samples were collected by Dr. Hannu Haapasalo and Dr. Joonas Haapasalo at Fimlab laboratories and measured with the approval of the Regional Ethics Committee of Tampere University Hospital.

4.1 Particle measurements

The electric particle filter is a crucial part of the measurement system and at the same time the only part that is not commercially available (at the time of writing this thesis, August 2017). This also means that it is the only part of the system that has not been subjected to extensive experimental research. Its novelty and importance in creating the ultimate target application for intraoperative cancer margin detection were the reasons why particle measurements with the electric filter were chosen as the first measurement set.

In order to thoroughly investigate the efficiency of the electric filter, the particle comparison between the cases, where the filter was active (ON), and where it was inactive (OFF), were done in three different ways. First the filtration efficiency was evaluated visually by color intensity analysis of glass fiber high efficiency particulate air (HEPA) filters (grade 691, 9.0 cm diameter, VWR International, U.S.A.). HEPA is a term used for filters, which can filter at least 99.97 % of 0.3 µm particles [48]. The second evaluation method relied on the mass change of the HEPA filters, and finally the third method was a quantitative analysis of particle mass and number distributions by using the ELPI® system.

The HEPA filter measurements were relatively simple, and the visual evaluation and mass based evaluation were executed concurrently with the same filters. First, a HEPA filter

was placed inside a steel casing which had an inlet and an outlet port. The casing was then connected to the sample outlet port of the electric filter, and no other alterations were done to the main measurement system. With the HEPA in place, a total of eight surgical cuts were made to a piece of kidney from a Finnish Landrace pig. The cuts were 5 mm long, 2.35 mm wide, and the power of the diathermy knife was set to 120 W (mode: 100 % cut). The depth of the cuts varied slightly depending on the shape and height of the tissue piece. The cutting pattern and its effect on the tissue sample can be seen in Figure 14.

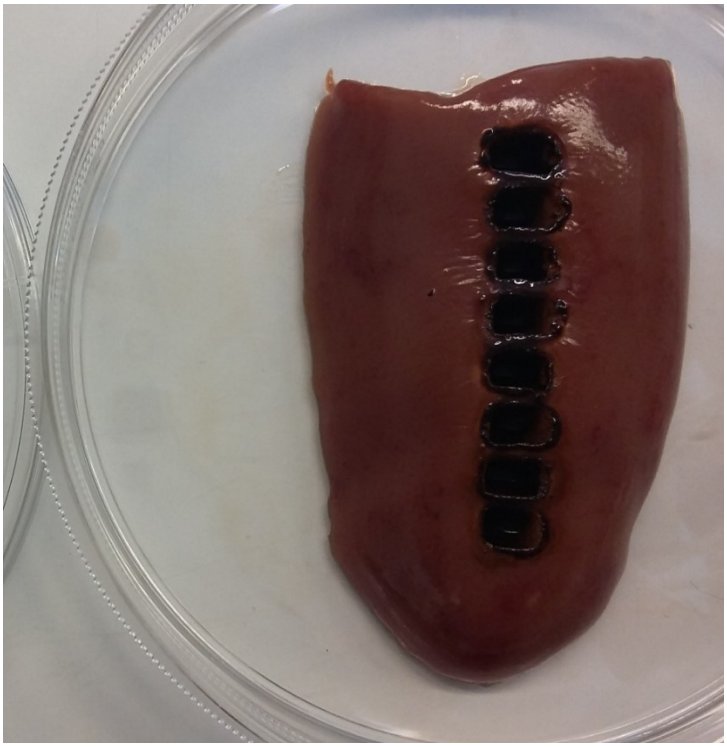

Figure 14. *A piece of porcine kidney after the cutting sequence in the first particle measurement set. The cutting sequence started from the bottom of the tissue piece and ended after the topmost cut.*

After the eight cuts were made, the HEPA filter was removed from the metal casing and placed inside a petri dish. The process was then repeated with 9 additional HEPA filters. In the case of the first five HEPA filters, the electric particle filter was inactive, and it was turned on for the last five HEPA filters. All HEPA filters and tissue samples were weighed with the XR 205SM-DR semi-micro balance before and after the electrosurgical cutting. After the ten filters were subjected to the diathermy smoke, they were scanned, first all at once, and then individually with the Epson Perfection 4870 Photo scanner with identical settings for each filter. The scanning was made against a white paper background. The scan resolution for the individual scans was 9600×9600 pixels and the images were saved with 16-bit color-coding in Tagged Image File Format (TIFF) in order to get high quality files for the color intensity inspection.

The quantitative analysis of mass and number distributions with the ELPI® system were done after the HEPA measurements. The ELPI® system was borrowed from the Department of Physics at TUT and the measurements were done in co-operation with postdoctoral researcher Sampo Saari. The particle filtration efficiency of the electric filter was examined by a simple experiment, where the state of the electric filter was alternated between active and inactive between electrosurgical cuts to pig liver. The cuts were approximately 4 mm deep, 5 mm long, and 2.35 mm wide. Due to the high number of particulate matter in the raw sample gas, the ELPI® system saturated to its maximum current value, when there was no dilution and the electric filter was inactive. In order to increase the dynamic range of the measurement, the sample gas created by electrosurgical cutting was guided towards the ELPI® by using an ejector diluter (Dekati Diluter DI-1000, Dekati Inc., Finland). The ejector diluted the sample gas at a ratio of approximately 1:8.6, after which it was further diluted with a side flow to a total dilution ratio of 1:45. The dilution gas was pressurized air from TUT's central pipelines. The ELPI® system was set to measure the particle distribution from the diluted sample flow at the end of the measurement setup. A schematic representation of the particle distribution measurement setup is visible in Figure 15.

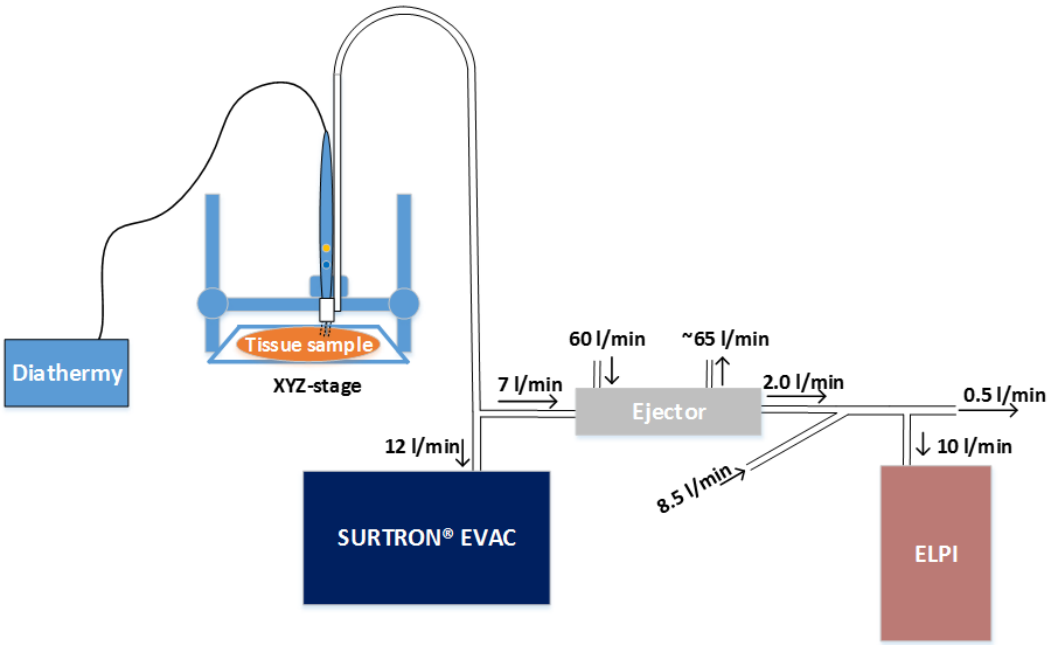

Figure 15. *Schematic illustration of the measurement setup used in the particle distribution measurements. The electric filter was added before the ejector in the filter validation experiment. The flow direction of sample gas is depicted with arrows and the value of the flow rate can be seen beside them. The waste flow (0.5 l/min) was guided to a fume hood.* [92]

The use of the ELPI® system in the filter experiment offered the possibility to add scientific value to the research by conducting another measurement set. The diathermy smoke is known to be hazardous to the operating staff, but the distinction between different tissue plumes has not been examined in many publications. The goal of the additional particle measurement set was to measure the particle mass and number distributions in the case, where ten different tissue types were subjected to identical pattern of electrosurgical cutting. The measurements were done after the electric filter validation test with the measurement setup seen in Figure 15. In addition to liver, the other tissues were skeletal muscle, fat, bronchus, renal pelvis, renal cortex, lung, gray matter, white matter, and skin. All tissues used in the measurement were from the same animal. The results of all particle measurements are presented in chapter 5.

4.2 Tissue identification measurements

After validating the function of the electric particle filter and having the preliminary experience in measuring various tissues in the particle measurements, the next major step in the research was to test the function of the full measurement system in tissue identification. However, before moving on to cancer detection, a proof-of-concept study with pig tissues had to be made to see, if the core principle of diagnosis through diathermy smoke ion mobility analysis, is even possible with our system. Since cancers are practically uncontrollable samples of the tissues they affect, the identification of the most common healthy tissues is relevant. If healthy tissues can be identified, it supports the hypothesis that cancer identification is also possible. In addition, the availability of porcine tissues is superior to human tissues due to obvious ethical constraints, and that is why they were far more suitable in the early phases of system development. The decision to use porcine tissues in favor of other animal tissues can be justified by its biological similarities with human tissues (size and genetics), and their usage in previous scientific publications as models for human physiology and anatomy [95–97]. The main measurement system with the electrosurgical sampling unit, the electric filter, and ENVI-AMC® was used in all tissue identification measurements.

At the beginning of the measurement set, the parameters of the system, such as dilution ratios, duration and resolution of DMS measurements, and cutting parameters were not optimized. That is why, during the thesis project, the tissue identification measurement protocol underwent many changes as a result of iterative experimentation. After the iteration process, parameters that were adequate in terms of measurement dynamics and resolution were found, with which three larger sets of tissue identification measurements were done. The power of the smoke evacuator was set to level 5, which equals approximately 12 l/min of raw sample flow. The combined dilution ratio of the two-stage ejector dilution system was 1:768. The voltage of the electric filter was set to 5.0 kV and the power of the diathermy knife to 120 W (mode: 100 % cut). The cuts were 4 mm deep,

5 mm long, and 0.5 mm wide. Some slight cutting depth variations due to the structural heterogeneity of certain tissue samples occurred during the measurement sets. The DMS measurement duration was approximately 12 seconds. V_C in the DMS sweeps was set to rise from -0.8 V to 9 V in 40 increments, and V_{RF} from 440 V to 700 V in 4 increments. This means that the resolution of the DMS dispersion plots was 40×4 (160 pixels). A three-minute cleansing period after each DMS measurement was added to the cutting protocols to ensure that the ENVI-AMC® would not measure any residual ions from the previous sample. All tissues were photographed with a Samsung A3 mobile phone camera (Samsung, South-Korea) before and after the electrosurgical cutting for visual reference for the classification of the results.

The first measurement set after the parameter iteration was a pilot test with five tissues: skeletal muscle, fat, lung, renal cortex, and liver. The tissues were measured shortly after acquiring them from the slaughterhouse, eliminating the need to freeze them in between. To prevent excess consecutive cutting of the same sample tissue, the tissue pieces were all placed on the CNC machine platform at the same time, and measured with one continuous tissue-alternating automated sequence. 2 cm wide tissue slices were placed as close to each other as possible, and 10 cuts were made to each slice. The automated cutting protocol was designed so that the number of consecutive cuts to each sample was only two, after which the next two cuts were made to another piece. In addition to the 50 tissue cuts, 10 measurements without tissue contact were made to get the baseline reference. An unscaled sketch of the cutting protocol is presented in Figure 16.

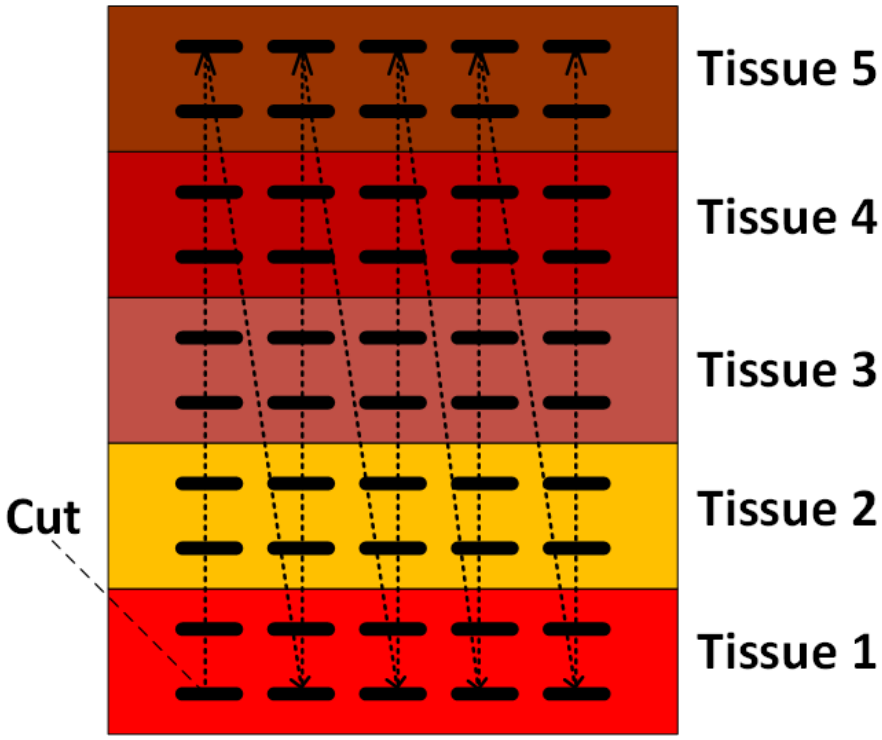

Figure 16. *A sketch of the cutting protocol for the tissue identification pilot test. Ten empty cuts, where the surgical knife did not touch anything but air, were also done for reference. The dashed arrow lines show the order of the incisions.*

After the successful pilot test, the sample size was increased with additional measurements to increase the statistical validity of the results. The number of different tissues was also increased. The added tissues were cerebral gray matter and white matter, skin, tongue, and heart. The aim was to increase the sample size to 60 measurements per tissue, but in some cases, the size of the tissues was a restricting factor. The cuts to gray matter had to be done to brains from four separate animals, and white matter measurements needed the brains of ten swine. All other measurements were done by using tissues from a single animal. An example of a tissue piece after one full measurement sequence in the second phase of the tissue identification measurements can be seen in Figure 17. Unlike in the pilot tissue identification measurements, the tissues had to be frozen in between measuring different tissues to prevent them from rotting. During a measurement sequence, we tried to prevent the excessive drying of the tissue piece by moisturizing it with a spray bottle filled with deionized water.

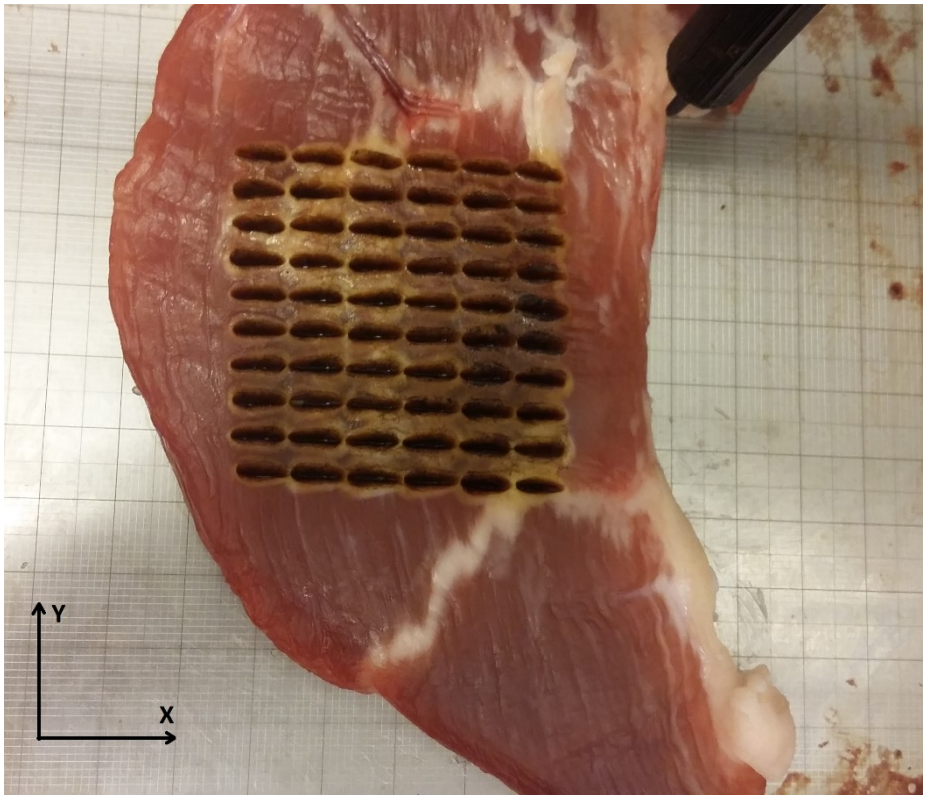

Figure 17. *A piece of pig skeletal muscle tissue after a full measurement sequence (60 cuts) in the additional tissue identification measurements. The left bottom corner was cut first, which was followed with nine additional cuts in the Y-direction with 3 mm gaps between each cut. After the 10th cut was made, the knife returned to its starting position, moved 6 mm to the X-direction, and started another set of ten Y-directional cuts.*

The growing of the sample size was a lengthy process, which spanned over multiple weeks. Even though the most important parameters were monitored and kept the same over the whole measurement period, some variation between the measurement conditions might have occurred over time, which in turn could have jeopardized the comparability of the measurement results. To account for the possible inter-day variations, a small independent validation set with skeletal muscle, fat, renal cortex, and liver was done, after the sample size in all measured tissues was at least 60. The decision to include these specific tissues in the validation measurement stemmed from the over-abundance of the tissue matter after the previous measurements. The measurement parameters in the validation set were the same as in the previous tissue identification measurements, except for the cutting protocol, which was done without an automated sequence. Each cut was made manually in a randomized order with no consecutive cuts to the same tissue type. The number of cuts in the validation set was 10 per tissue, resulting in a total number of 40 measurements. The results from the pilot, additional, and validation measurement sets are all presented in chapter 5.

4.3 Diathermy measurements with brain tumors

After testing the measurement system in the tissue identification measurements with healthy porcine tissues, the system was deemed ready for tumor identification. For the thesis research, we were able to acquire a small set of brain tumor samples for a pilot test. The samples were gathered with the help of docent of neuropathology Hannu Haapasalo, M.D. Joonas Haapasalo, and medical student Ilkka Haapala. Haapala was also assisting in the actual measurements. A total of 14 brain tumor samples were collected. Half of the samples were meningiomas and the other half were glioblastomas.

Considering the scarceness of available material and ethical aspects in using human tissue, the effective use of the samples was of paramount importance. To maximize the usage of sample tissue, a well plate for holding the sample pieces was designed with SOLIDWORKS® 3D computer-aided design software (SolidWorks Corporation, U.S.A.). The use of a well plate was also beneficial in controlling the depth of the incisions and keeping the colloidal brain matter from spreading and flattening on the platform. The wells were rectangular with rounded edges. The bottom of each well was also rounded. The exact dimensions of the well plate in millimeters can be seen in the SOLIDWORKS® drawing in the upper part of Figure 18.

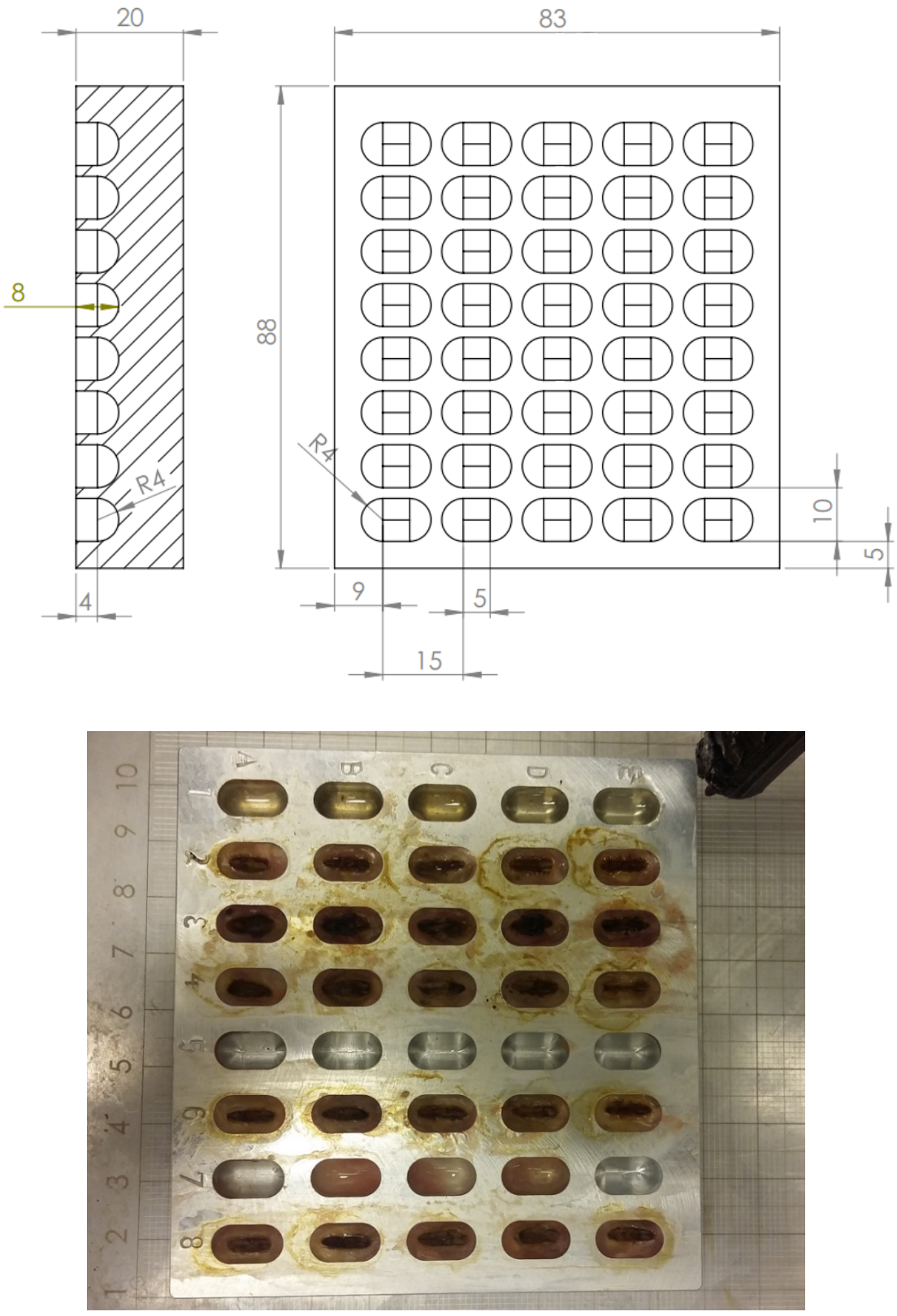

Figure 18. *A SOLIDWORKS® drawing of the well plate used in the brain tumor identification measurements (top), and the well plate after a test measurement sequence with porcine brain samples (bottom). The numbers in the drawing show the dimensions in millimeters.*

The well plate and the cutting protocol were tested with pig brains before the tumor measurements. A picture of the well plate after the test measurement sequence can be seen in Figure 18 (bottom). The cuts were the same 5 mm long and 4 mm deep line cuts as in the previous measurements. The power of the smoke evacuator was also set to level 5. The dilution ratio was changed to 1:472, since it seemed to work adequately well in the test measurements. The DMS measurement duration was shortened to approximately 10 seconds, but the resolution of the positive and negative sweeps was kept the same as in the tissue identification measurements (160 pixels).

The tumor samples varied in size. Some of the tumor samples were too small for even one 4 mm cut, while some were large enough to be split into two or three wells. To maximize the number of measurements, almost all sample pieces were burned from two sides. After the first cut was done to a set of samples, the pieces that were big enough were turned upside down and cut a second time. From the 14 sample pieces, a total of 43 measurements were done. In addition, 4 empty cuts were made for reference. The results of the brain tumor measurements are presented in the next chapter.

5. RESULTS AND ANALYSIS

The most important findings from the pivotal measurements are introduced in this chapter. Due to its novelty and overall importance to the proper function of the measurement system, the results from the particle measurements with the electric filter are presented thoroughly in three parts (mass change, color intensity and particle distributions from the ELPI® data). The main findings of the particle distribution measurements with different tissues are also briefly described; a more detailed analysis of the results is presented in a journal article, which was concurrently written with this thesis [92]. The electric filtration solution and the tissue identification measurements will also be subjects for a journal article, but their results are more relevant regarding the objectives of this thesis research, so they will be discussed in more detail. Lastly, the results of the brain tumor measurement pilot test are also introduced and analyzed.

5.1 Filter validation and particle distributions

In the particle measurements where the efficiency of the electric filter was studied, five glass fiber HEPA filters were first subjected to diathermy smoke, when the filter was inactive. After that, the electrosurgical cutting was done with the electric filter active. The group scan of the glass fiber HEPA filters used in the particle measurements is shown in Figure 19.

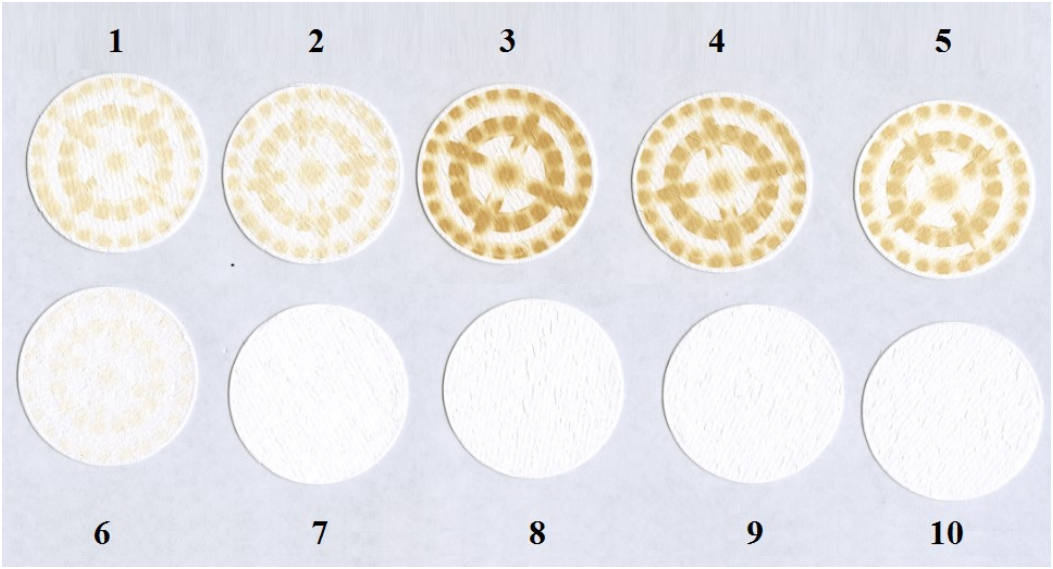

Figure 19. *A scanned image of the glass fiber filters used in the particle measurements. Filters 1−5 were in the measurement system, when the electric particle filter was inactive, and 6−10 were in the system, when the electric filter was active. The contamination is only partial due to the steel casing used in the measurements.*

By looking at the scanned glass fiber filters in Figure 19, it is rather obvious just by visual inspection that using the electric filter greatly reduces the contamination. To support this claim, color intensity analysis from the individual scans was conducted by using the custom-made MATLAB-based image processing algorithm described in chapter 3. Color intensity histograms from the observed area for each filter are presented in Figure 20.

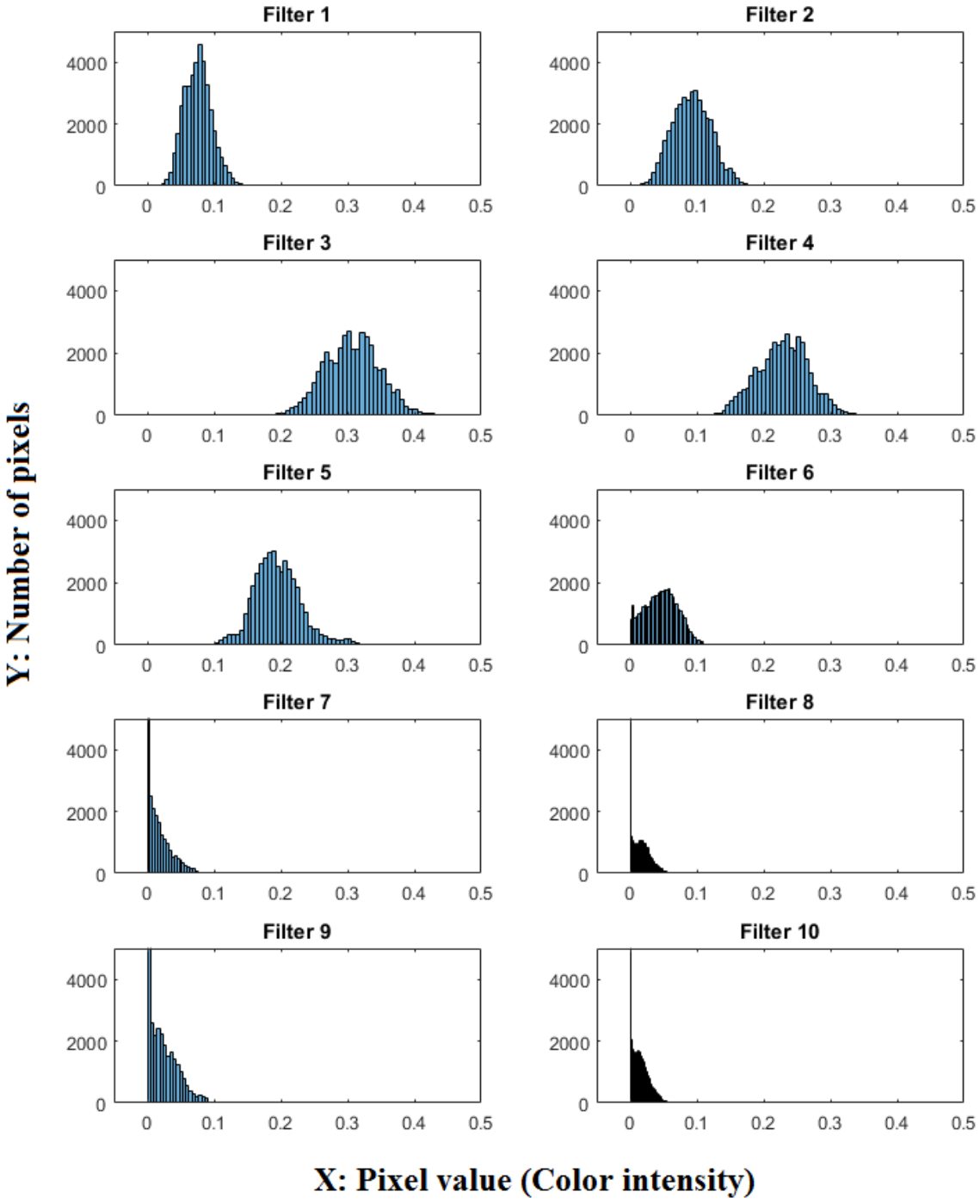

Figure 20. *Color intensity histograms of the glass fiber filters used in the electric filter validation particle measurements. The color intensity value is reversed as opposed to normal grayscale images, which means that a higher value equals a darker shade.*

As can be seen in Figure 20, the first five filters have significantly darker pixel distribution than the last five filters. It also seems that filter number 3 is the most contaminated based on the histograms. All the filters that were in the system, when the electric particle filter was active, have a small number of dark pixels, which means that they have remained uncontaminated. However, the histograms reveal some contamination in filter number 6, even though the electric filter was active. The surgical cuts made in that particular measurement were exceptionally deep, which in turn created more smoke. These results indicate that there might be some loss of particle filtration efficiency in the electric filter, if the filter is subjected to extremely high smoke concentrations.

To have more insight on the function of the electric filter, a quantitative analysis based on the contamination metric can be made. For this purpose, all of the glass fiber HEPA filters and tissue pieces were also weighed to see the relation of mass changes between them. The mass increase and the values of the contamination metric for each filter, in addition to mass decrease of each tissue piece as a result of the electrosurgical cut, can be seen in Table 3.

Table 3. *Values for the increase of filter mass, the decrease of tissue mass, and contamination metric for each glass fiber filter in the electric particle validation measurements. The mass of the first tissue piece is crossed over due to the value being unreliable, because of excessive drying.*

Filter/Tissue	Mass increase of filter (mg)	Mass decrease of tissue (g)	Contamination metric (sum of pixel values)
1	0.35	~~0.92~~	3039.43
2	0.47	0.74	3704.24
3	2.24	1.85	12272.00
4	1.77	1.38	9168.63
5	1.20	1.11	7809.44
6	0.05	1.71	1871.69
7	0.01	1.19	374.75
8	0.00	1.38	367.47
9	0.04	1.23	654.66
10	0.01	1.06	467.72

Based on the values in Table 3, a graph showing the contamination metric as a function of the mass decrease of tissue is presented in Figure 21. Similarly, a second graph showing the mass increase of the filter as a function of the mass decrease of the tissue is presented in Figure 22. The mass of the first tissue piece was measured with a significant approximately 30-minute long delay, during which the tissue had lost a noticeable amount

of weight through dehydration. Therefore, the first tissue-filter pair is neglected in the graphs.

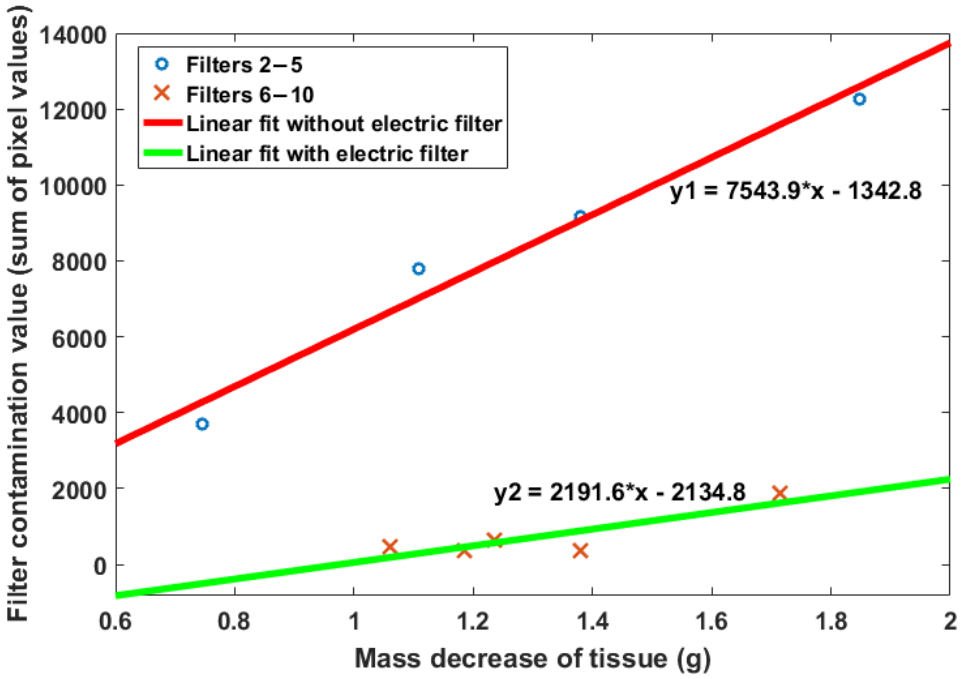

Figure 21. *Filter contamination as a function of the electrosurgically removed tissue mass. The data points and their linear least square fit curves with equations are visible.*

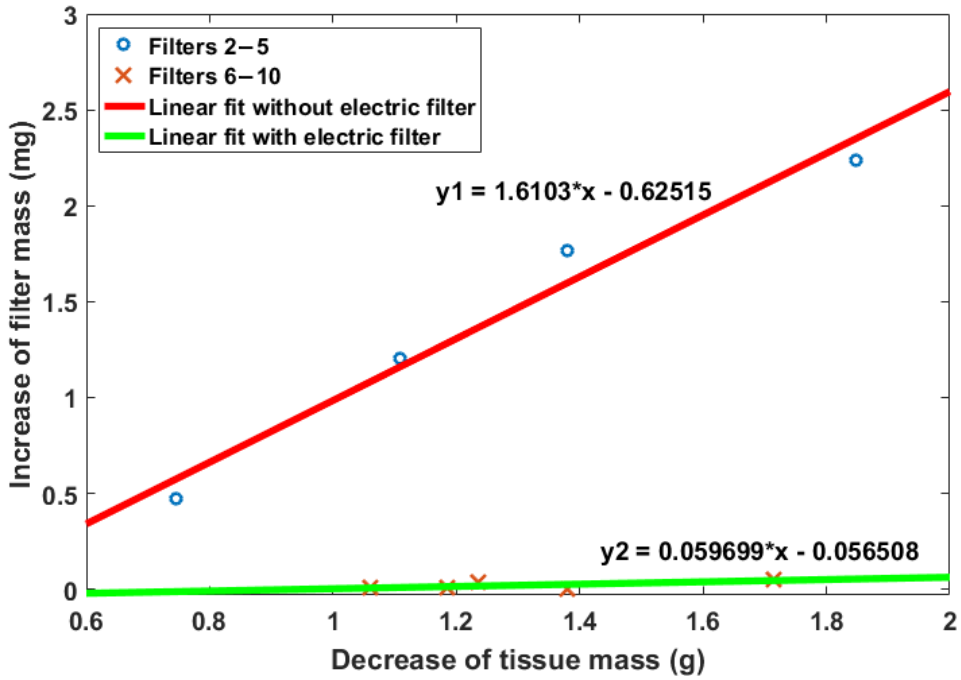

Figure 22. *Increase of filter mass as a function of the electrosurgically removed tissue mass. The data points and their linear least square fit curves with equations are visible.*

Both Figure 21 and Figure 22 show clearly that the electric filter works well in preventing the contamination of the measurement system. The slope of the least squares linear fit of the data groups in both figures was significantly lower, when the electric filter was active. However, the most conclusive proof of its effectiveness can be seen in the ELPI® data. The signal response of the ELPI® dropped to its detection limit, when the electric filter was active and surgical smoke from liver tissue was guided into the system. This means that the signal from the measurement cannot be distinguished from noise. If the raw data from the measurement is presented alongside measurement data without the electric filter as particle number and mass distributions, the effectiveness of the filter becomes evident, as can be seen in Figure 23.

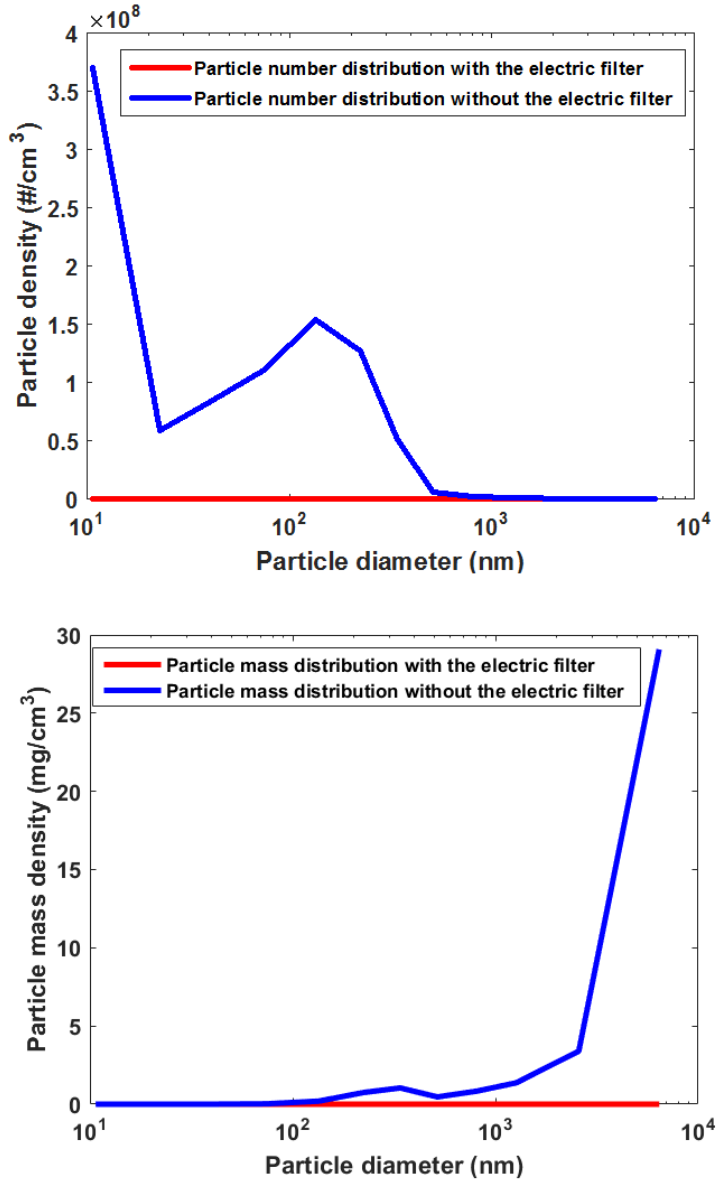

Figure 23. *Particle number and mass distributions for liver in relation to particle diameter, with and without the electric particle filter.*

If the particle filtration efficiency is evaluated numerically from the ELPI® data by means of particle number density comparison, we can formulate:

$$\eta_{filter} = 1 - \frac{N_{ON}}{N_{OFF}} = 1 - \frac{2.3540 \cdot 10^4 cm^{-3}}{2.7583 \cdot 10^8 cm^{-3}} = 0.99991 \ldots \approx \mathbf{99.99}\ \%, \qquad (7)$$

where η_{filter} is the particle filtration efficiency of the electric filter, N_{ON} is the median particle number density of liver tissue measurement when the electric filter is active, and N_{OFF} is the median particle number density of liver measurement when the electric filter is inactive. The value of the filtration efficiency is potentially even higher than the calculated result, since the restricting factor in the formula is the value of N_{ON}, which is already at the detection limit of the ELPI® and thus cannot not be distinguished from noise.

The ELPI® system was also utilized in a measurement set that does not directly coincide with the objectives of this thesis research. However, it did provide critical information about workplace safety for surgeons and useful information on the differences of the particle smokes from various tissues. The results revealed that the tissues could be divided into three distinct classes based on the amount of particulate matter (PM) created in electrosurgery, and by extension, hazardousness of their surgical smoke. The proposed classes are: low-PM tissues (fat, gray matter, white matter, skin, bronchus), medium-PM tissues (renal cortex, renal pelvis, skeletal muscle), and high-PM tissues (liver). In practice, these results could be useful for the surgeon and assisting personnel in the operating staff, when preparing for a surgical operation. The class of the operated tissues would help when considering for example what kind of surgical masks are needed in order to prevent lung deposition of particulate matter during the operation. A more thorough look at the particle distributions from different tissues and their implications to workplace safety for surgical staff can be found in the article that was submitted during the thesis work [92].

The visual inspection, color intensity analysis, mass comparisons, and particle measurements with ELPI® all show that the electric filter works exceptionally well in preventing the contamination of the measurement system. Based on the ELPI® measurements, we can say that the filtration efficiency of particles in the diameter range of 7 nm to 10 µm, is at least 99.99 %. When also considering that the most probable contaminates in tissue plume are in the size region of 1 nm to 10 µm [47, p. 2], we can conclude that the filter works especially well in this application.

5.2 Tissue identification

In the tissue identification measurements, the aim was to measure and compare the molecular structure of the diathermy plume from different porcine tissues with the ENVI-AMC®. Three separate measurement sets (initial pilot test, growing the sample size, and validation) were executed. The data from the ENVI-AMC® was classified in MATLAB by using LDA with LOOCV.

The data fed to the LDA classifier from each measurement had 160 values, based on which the algorithm tried to classify the sample as one of the known tissue types. After each sample in the measurement set was classified, the algorithm created a confusion matrix, which shows the full set of the classification results.

In the pilot tissue identification set, ten DMS measurements from the tissue smoke of skeletal muscle, fat, liver, renal cortex, and lung were done. Reference data with ten empty cuts were also gathered. The confusion matrix from the classification results is presented in Table 4. The classification was done by using both the negative and the positive DMS channel data. The percentage of correct classifications was **93.33 %**.

Table 4. *The confusion matrix from the LDA + LOOCV classification results in the tissue identification pilot test. CCR: 93.33 %.*

Tissue	Muscle	Fat	Renal cortex	Liver	Lung	Empty
Muscle	**10**	0	0	0	0	0
Fat	0	**10**	0	0	0	0
Renal cortex	0	0	**9**	**1**	0	0
Liver	0	0	**3**	**7**	0	0
Lung	0	0	0	0	**10**	0
Empty	0	0	0	0	0	**10**

In Table 4, we see that one renal cortex sample was classified as liver, and three liver samples were classified as renal cortex. The reason for the misclassifications might be that both tissue types produced a high concentration of smoke that partly saturated the DMS system. The saturation can be seen as the total disappearance of the reactant ion peak and the dominance of the heavy VOCs ($V_C = 0$) in the dispersion plots of both

tissues. The dispersion plots can be seen in Figure 24. For comparison, an unsaturated example of a dispersion plot from fat is also presented beneath the saturated responses.

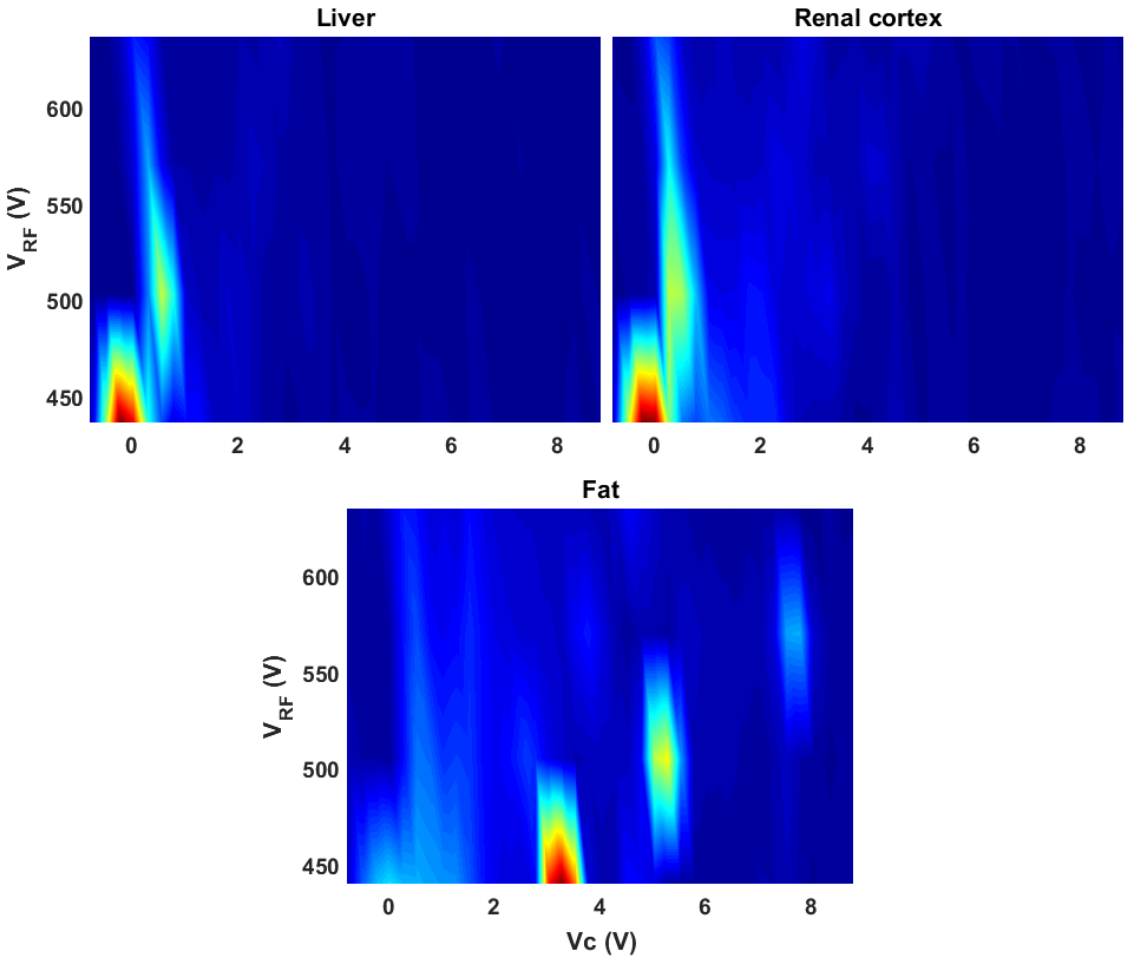

Figure 24. *Example dispersion plots of liver and renal cortex displaying the saturation effect in the tissue identification pilot measurement set. The response for fat is not saturated, and thus the RIP is visible in the bottom plot.*

Despite the few misclassifications, the overall results from the pilot test were extremely promising, since they clearly indicated that reliable differentiation of diverse tissue types could be possible with the measurement system. To increase the statistical validity of the hypothesis, additional 60 measurements to each tissue type were made. The number of different tissues was also increased. In some measurements, the negative sweep was corrupted, which resulted in the overall decrease of the CCR. That is why the classifications were done by only using the positive channel. The classification results in the form of LDA + LOOCV confusion matrix are presented in Table 5. The percentage of correct classifications was **95.33 %**.

Table 5. *The confusion matrix from the LDA + LOOCV classification results in the additional measurements in tissue identification. CCR: 95.33 %*

Tissue	Gray matter	White matter	Liver	Muscle	Fat	Lung	Renal cortex	Skin	Tongue	Heart
Gray matter	**60**	0	0	0	0	0	0	0	0	0
White matter	**1**	**59**	0	0	0	0	0	0	0	0
Liver	**1**	0	**59**	0	0	0	0	0	0	0
Muscle	0	0	0	**55**	**2**	**2**	**1**	0	0	0
Fat	0	0	0	0	**60**	0	0	0	0	0
Lung	0	0	0	0	0	**56**	**2**	0	**2**	0
Renal cortex	0	0	0	**1**	0	**4**	**53**	0	**2**	0
Skin	0	0	0	0	0	0	**1**	**58**	**1**	0
Tongue	0	0	0	0	0	0	**6**	**1**	**52**	**1**
Heart	0	0	0	0	0	0	0	0	0	**60**

Considering the large number of different tissue types, the percentage of correct classifications is especially impressive. Still, some misclassifications can be seen in Table 5. Renal cortex and tongue had the most misclassified samples (7 and 8, respectively). In the case of renal cortex, some of the cuts also hit renal pelvis by mistake, which might have led to different smoke composition, which could in turn account for the classification errors. The heterogeneity of the sample pieces is the most probable factor for the other misclassifications. For example, some lung tissue pieces had some hematomas that affected the DMS response. The heterogeneity is also somewhat visible in Figure 17, where some of the cuts have clearly been made to parts of the skeletal muscle tissue, where there is a lot of intramuscular fat. The low resolution of the DMS measurement could also explain some of the misclassifications. With 160 pixels, the amount of data is limited and thus, small differences in the composition of tissue smoke might not show up clearly in the dispersion plot. Also, due to being inside the fume hood for hours during a measurement sequence, some of the tissues dried up to some degree despite the spray

bottle watering. In earlier experiments, it seemed that dried tissue produced more smoke as opposed to fresh moist tissue, which could also partly explain the errors in classification.

After the classification of the additional measurement set, it seemed clear that the system is capable of reliable tissue identification. However, some distortion of the results could have happened due to possible inter-day variability of measurement conditions, for example temperature, flow rates, or pressure values. That is why a validation set of ten measurements with four tissues (renal cortex, fat, muscle, and liver) was executed. The classification results are presented in Table 6. The CCR was consistent with the pilot test and additional measurement set, with a value of **95.00 %.**

Table 6. *The confusion matrix from the LDA + LOOCV classification results in the validation set in tissue identification. CCR: 95.00 %.*

Tissue	Renal cortex	Fat	Muscle	Liver
Renal cortex	**9**	0	**1**	0
Fat	0	**10**	0	0
Muscle	0	0	**9**	**1**
Liver	0	0	0	**10**

Again, the single misclassifications for muscle and renal cortex can potentially be explained by the low resolution of the DMS measurement or the heterogeneity of the electrosurgically cut sample piece. Despite that, the results of the validation set confirmed that the system works in tissue identification, and consequently opened the way for tumor identification.

5.3 Tumor identification

After the success of the tissue identification measurements, the decision to move on to testing the capability of the system in actual tumor identification could be done with relative confidence. The measurement principle was the same as in porcine tissue identification: measure and compare the molecular structure of the diathermy plume from the tissues with the ENVI-AMC®. Due to the slim availability of brain tumor samples in the Pirkanmaa region, only a pilot test with 14 (7 meningiomas and 7 glioblastomas) sample pieces could be done at the time. From the 14 pieces, 43 measurements were made (and four empty cuts for reference).

The first analysis of the tumor measurement data was done without pre-existing knowledge of the actual tissue types in each measurement (except for empty cuts). This means that the supervised LDA or the kNN methods would not work in the classification. However, hierarchical clustering to the measurement data can be done even without any knowledge of how many separate sample groups were present and what was the number of samples in each of them. A dendrogram from the measurement data can be seen in Figure 25.

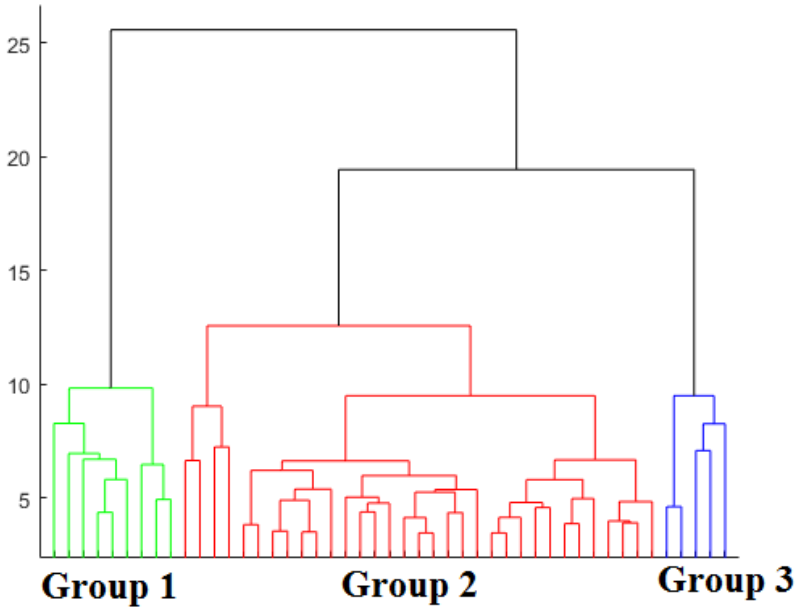

Figure 25. *Dendrogram of the brain tumor measurements.*

As can be seen from the dendrogram in Figure 25, three separate data clusters are visible, which could indicate that the classification to meningiomas, glioblastomas, and empty cuts is at least partly successful even with blind analysis.

The actual types of the samples were revealed after the blind analysis of the measurement data was done. The hierarchical clustering based classification to three groups from the dendrogram seemed to have worked quite poorly with only 49 % CCR. Still the percentage is better than the average CCR of 33 % in a situation where the three classes would be decided completely randomly. However, blind analysis without prior information is not the best way to process DMS data in this case due to the incision depth induced intensity changes in the signals. That is why the results from the more feature-sensitive supervised classification methods (LDA and kNN) are more conclusive. In previous tissue identification measurements, the LDA classification produced slightly better results than the kNN, but in the tumor pilot, the roles were reversed. The classification with LDA resulted in CCR of 72.3 %. The classification with 2-nearest neighbors produced an even higher value of **85.11 %**. The confusion matrix from the kNN classification is presented in Table 7.

Table 7. *The confusion matrix from the kNN + LOOCV (k = 2) classification results in the brain tumor measurements. CCR: 85.11 %.*

Tissue	Meningioma	Empty	Glioblastoma
Meningioma	**21**	**1**	**4**
Empty	0	**4**	0
Glioblastoma	**1**	**1**	**15**

The results in Table 7 are highly significant. The pilot test indicates that the differentiation of two types of brain tumors is possible with the measurement system. In these measurements, the size of the samples varied significantly, which resulted in different incision depths, and by extension, different amount of smoke. The maximization of used tissue by doing second cuts to the same pieces might have also distorted the results, since some cutting of already potentially charred tissue was inevitable. On the other hand, some of the samples were extremely small, which resulted in the surgical knife only grazing the surface. This is most probably the reason for one meningioma and one glioblastoma being classified as ‘’Empty”. Considering the suboptimal conditions of the measurement set, the results are surprisingly good.

If we were to use the system for a test where the aim is to detect the malignancy of a brain tumor, the results from the pilot measurement could be used to calculate the sensitivity and specificity along with the positive and negative predictive values. In this case, positive test result would mean that the subject has glioblastoma and a negative test result would mean meningioma. For the calculation, the empty cuts are not relevant, therefore the evaluation is done with only the 43 measurements that actually were from the cuts to tissue pieces. The diagnostic parameters are presented in Table 8.

Table 8. *Diagnostic table for the differentiation of glioblastoma and meningioma based on the brain tumor pilot measurements.*

	Glioblastoma	Meningioma	
Positive test result	TP = 15	FP = 4	PPV ≈ **78.9 %**
Negative test result	FN = 2	TN = 22	NPV ≈ **91.7 %**
	Sensitivity ≈ **88.2 %**	Specificity ≈ **84.6 %**	

As can be seen from Table 8, the diagnostic properties for the hypothetical malignancy test with the system are quite good, considering that it is based on the results of a pilot set. In a malignancy test like this, it can be argued that the number of false negatives is more important than the number of false positives. If the test is considered reliable and the result is positive, the physician-in-charge has the presumption that the patient has a malignant tumor. This leads to traditional tissue biopsy, where potential false positives will be screened out. The negative test result could however give the indication that treatment is not necessarily required, and if the diagnosis is false, the decision to discharge the patient or leave the tumor untreated, could be fatal. That is why especially the high values for NPV and sensitivity in Table 8 are important, and show promise that the system has potential to be used in diagnosing the malignancy of the operated tumor.

When comparing these results to those achieved with REIMS, the need for improving the system in terms of sensitivity and specificity can be argued. Balog et al. achieved over 95 % sensitivity and specificity for the cancer-or-healthy classification with all tested tissue types [9]. However, the small sample size of 14 tumors in our pilot study compared to the over 300 in the publication, precludes the possibility for statistically reliable conclusions of the performance differences of REIMS and our system. Furthermore, the sensitivity and specificity are not directly comparable, since the brain tumor measurements in this thesis were done without healthy control samples. Until further research and measurements are conducted, the performance comparison is groundless, but based on the results, the potential for creating a method that can compete with REIMS, is clear.

The use of healthy human brain tissue is practically impossible in this type of scientific pilot research, since there are no easily available samples from living subjects for obvious reasons. Still, without healthy tissue samples, the measurement results do not directly prove the system's capability to distinguish healthy brain tissue from cancerous tissue. However, based on all of the tissue measurement results, we can assume with relative confidence that it is possible. In the case of malignant brain tumors, the tumor can almost never be fully excised by using electrosurgery due to infiltration of the tumor to the supportive tissue [29]. Therefore, the cancer margin detection is not even as relevant as for example in the case of breast cancer. Intraoperative differentiation of malignant and benign brain tumor types is perhaps more relevant, and in that regard, the results are promising. As a whole, the results from all measurement sets were excellent, and they provided a good basis for further product development and significant scientific research.

6. CONCLUSIONS

The objective of this thesis research was to introduce, test, and partly validate a device that could be used in intraoperative cancer margin detection in the near future. Even though the system is not yet capable for latencies that could accommodate the intraoperative detection, the proof-of-concept is verified. The objectives were met and the groundwork for future research and development was done.

Based on the results of the particle measurements, it is clear that the electric particle filter works extremely well in filtering out the nanoscale and microscale particles, reaching a minimum filtration efficiency of 99.99 %. Since the particle size range of bacteria and viruses is in the upper nanoscale or microscale size region [47,98], it can be assumed that the filter will effectively prevent bacterial and viral contamination of the subsequent parts of the measurement system. In terms of micro-organisms inactivation through ozone-induced cell wall destruction, perhaps a more thorough test set with microbiological culturing from the filtered sample could be conducted to get conclusive results. With the parameters used in this research, the filter produces an estimated 0.5−2 ppm concentration of ozone, which is enough to destroy over 99 % of common bacteria and viruses in a water medium, but its effectiveness to inactivate airborne bacteria should be studied further [88]. The particle measurements also resulted in useful publishable information about the hazardousness of surgical plume from different tissues in electrosurgical operations [92].

The tissue identification measurements were successful in validating the concept of distinguishing different healthy tissues by DMS analysis from the diathermy smoke. Similar research has been done with MS before [39], but this is the first study with the more cost-effective and simpler DMS technology. The correct classification rate was consistently over 93 % in all measurement sets in porcine tissue identification.

The results from the tumor identification measurements further demonstrated the system's capability in differentiation of tissue types. Even though the measurement set was only a pilot test with suboptimal measurement conditions, two types of brain tumors, malignant glioblastoma multiforme and benign meningioma were distinguished with relative success (85.11 % CCR). However, the brain tumor measurement set also brought to attention some of the targets for future development.

The system used in these measurements was wasteful in terms of sample consumption. The current five second cutting protocol evaporates a lot of tissue (approximately 0.5−2 g depending on the incision depth) and creates a large amount of smoke, which contaminates the first parts of the measurement system rather quickly. Still, the sample is

consumed in less than twenty seconds, which means that the DMS measurement needs to be fast, which in turn leads to reduced scan resolution. In other words, the current system uses too much tissue too fast. Eventually, the system should be able to do qualitative analysis even from low-resolution data. However, at this point in development, we are still searching for the optimal parameters and distinctive features in the dispersion plots, which would be easier with higher resolution. To overcome this problem, the sampling efficiency needs to be improved. One way to achieve this is to have a sample chamber, which gathers the sample efficiently and fast, but which then empties more slowly, so that the DMS measurement can take longer. This type of solution is more complicated than the straightforward current method, but almost imperative, when considering future research and the target application.

Even with a more efficient sampling method, the system would still be too sensitive to the intensity variations of the produced smoke. Intensity of the signal can be a parameter for classification when measuring different tissues, but the intensity changes due to the depth variations of the cuts are not favorable. This could be fixed with an automated dilution system that would, for example, make a rapid intensity check before the actual measurement, and then change the dilution coefficient (with an automated valve system) accordingly to maintain a constant sample intensity level.

Another downside of the current system is its size. Even though most of the operating theaters are large enough to accommodate the system in its current state, for practical reasons, some miniaturization must be done before moving on to tests in authentic surgical environment. Also, currently the measurement dynamics of the system are not optimized due to lengthy tubing. More space-effective component placement could make the measurement time of the system significantly faster, and at the same time it would make the system more compact and aesthetically pleasing. The system could then also be encapsulated, which would enable the simultaneous and effective heating of the pneumatics. This, in turn, could help in reducing the decontamination time of the system, since heating would dislodge particulate matter that has adhered to the PTFE tubes more effectively.

Despite its current shortcomings, the system proposed in this thesis is now at a phase in which its applicability in cancer detection is tentatively proven. When comparing this research to publications done by using REIMS, the results in cancer identification were slightly inferior, but the comparison of the performance is not relevant at this point, since the tumor measurements in this project were only a pilot test with a small sample size and no healthy control samples. The performance can be reliably estimated only after more studies with a larger sample size and varying protocols are conducted. However, when considering the differences in cost and complexity of the methods, the impact of the achieved results is significant, and show promise for the future of our system. The

introduced system is in a prototype phase, which means that it is in a constant state of evolution and progress. The next steps in development of the system offer the possibility for further scientifically significant research. Measurements with different types of cancer (especially breast cancer), the optimization of the sampling system, and parallel measurement modalities, alongside software and data analysis improvements moving towards real-time cancer detection, are all considerable subjects for new publications.

As a concluding statement, it is reasonable to say that the research was extremely successful and that its scientific impact was notable. The development of the measurement system will continue, and it will hopefully end in the creation of a commercial medical device that will revolutionize the field of intraoperative cancer margin detection.

REFERENCES

[1] American Cancer Society. Global Cancer Facts & Figures 3rd Edition. American Cancer Society. 2015;1–64.

[2] O'Kelly Priddy CM, Forte VA, Lang JE. The importance of surgical margins in breast cancer. Journal of Surgical Oncology. 2016;113:256–63.

[3] Waljee JF, Hu ES, Newman LA, Alderman AK. Predictors of Re-excision among Women Undergoing Breast-Conserving Surgery for Cancer. Annals of Surgical Oncology. 2008;15:1297–303.

[4] Wittekind C, Compton CC, Greene FL, Sobin LH. TNM residual tumor classification revisited. Cancer. 2002;94:2511–6.

[5] Emmadi R, Wiley EL. Evaluation of resection margins in breast conservation therapy: the pathology perspective—Past, present, and future. International journal of surgical oncology. Hindawi Publishing Corporation; 2012;2012.

[6] Massarweh NN, Cosgriff N, Slakey DP. Electrosurgery: History, principles, and current and future uses. Journal of the American College of Surgeons. 2006. p. 520–30.

[7] González-Bayón L, González-Moreno S, Ortega-Pérez G. Safety considerations for operating room personnel during hyperthermic intraoperative intraperitoneal chemotherapy perfusion. European Journal of Surgical Oncology. 2006;32:619–24.

[8] Ulmer BC. The hazards of surgical smoke. AORN Journal. 2008. p. 721–38.

[9] Balog J, Sasi-Szabo L, Kinross J, Lewis MR, Muirhead LJ, Veselkov K, et al. Intraoperative Tissue Identification Using Rapid Evaporative Ionization Mass Spectrometry. Science Translational Medicine. 2013;5:194ra93.

[10] Cornu JN, Cancel-Tassin G, Ondet V, Girardet C, Cussenot O. Olfactory detection of prostate cancer by dogs sniffing urine: A step forward in early diagnosis. European Urology. 2011. p. 197–201.

[11] Covington J a., van. der Schee MP, Edge a. SL, Boyle B, Savage RS, Arasaradnam RP. The application of FAIMS gas analysis in medical diagnostics. The Analyst. 2015;6775–81.

[12] CBRNE Tech Index. Differential Ion Mobility Spectrometry (DMS) [Internet]. [cited 2017 Jun 25]. Available from: http://www.cbrnetechindex.com/Chemical-Detection/Technology-CD/Spectrometry-CD-T/Differential-Ion-Mobility-Spectrometry-CD-S

[13] National Cancer Institute. "Cancer" [Internet]. NCI Dict. Cancer Terms. National Cancer Institute; [cited 2017 Apr 18]. Available from: https://www.cancer.gov/publications/dictionaries/cancer-terms?CdrID=45333

[14] Stewart BW, Wild CP. World Cancer Report 2014. World Health Organization. Geneva. 2014.

[15] National Cancer Institute. Cancer treatment [Internet]. [cited 2017 May 10]. Available from: https://www.cancer.gov/about-cancer/treatment/types

[16] Singletary SE. Surgical margins in patients with early-stage breast cancer treated with breast conservation therapy. The American Journal of Surgery. 2002;184:383–93.

[17] Breastcancer.org. Surgical Margins [Internet]. [cited 2017 Apr 20]. Available from: http://www.breastcancer.org/symptoms/diagnosis/margins

[18] Cendán JC, Coco D, Copeland EM. Accuracy of intraoperative frozen-section analysis of breast cancer lumpectomy-bed margins. Journal of the American College of Surgeons. 2005;201:194–8.

[19] Brown JQ, Bydlon TM, Richards LM, Yu B, Kennedy SA, Geradts J, et al. Optical assesssment of tumor resection margins in the breast. IEEE Journal on Selected Topics in Quantum Electronics. 2010;16:530–44.

[20] Pataky RE, Baliski CR. Reoperation costs in attempted breast-conserving surgery: A decision analysis. Current Oncology. 2016;23:314–21.

[21] HUS. Rintasyövän leikkaushoito [Internet]. [cited 2017 May 12]. Available from: http://www.hus.fi/sairaanhoito/sairaanhoitopalvelut/rintarauhaskirurgia/rintasyopaleikkaus/Sivut/default.aspx

[22] Fisher B, Anderson S, Bryant J, Margolese RG, Deutsch M, Fisher ER, Jeong JH WN. Twenty-Year Follow-Up of a Randomized Trial Comparing Total for the Treatment of Invasive Breast Cancer. The New England Journal of Medicine. 2002;347:1233–41.

[23] Jatoi I, Proschan M a. Randomized trials of breast-conserving therapy versus mastectomy for primary breast cancer: a pooled analysis of updated results. American journal of clinical oncology. 2005;28:289–94.

[24] Cardoso F, Costa A, Senkus E, Aapro M, André F, Barrios CH, et al. 3rd ESO–ESMO international consensus guidelines for Advanced Breast Cancer (ABC 3). The Breast. 2016;31:244–59.

[25] American Brain Tumor Association. Astrocytoma [Internet]. [cited 2017 May 13]. Available from: http://www.abta.org/brain-tumor-information/types-of-tumors/astrocytoma.html

[26] Kumar V, Abbas AK, Aster JC. Robbins and Cotran pathologic basis of disease. 9th ed. Elsevier Saunders; 2015.

[27] Thakkar JP, Dolecek TA, Horbinski C, Ostrom QT, Lightner DD, Barnholtz-Sloan JS, et al. Epidemiologic and molecular prognostic review of glioblastoma. Cancer Epidemiology Biomarkers and Prevention. 2014;23:1985–96.

[28] Wiemels J, Wrensch M, Claus EB. Epidemiology and etiology of meningioma. Journal of Neuro-Oncology. 2010;99:307–14.

[29] DynaMedPlus. Glioblastoma [Internet]. [cited 2017 Jun 1]. Available from: https://www.dynamed.com/topics/dmp~AN~T116043

[30] Nguyen FT, Zysk AM, Chaney EJ, Kotynek JG, Oliphant UJ, Bellafiore FJ, et al. Intraoperative evaluation of breast tumor margins with optical coherence tomography. Cancer Research. 2009;69:8790–6.

[31] Olson J, Sharp P, Goatman K, Prescott G, Scotland G, Fleming A, et al. Improving the economic value of photographic screening for optical coherence tomography-detectable macular oedema: a prospective, multicentre, UK study. Health Technology Assessment. 2013;

[32] Nolan RM, Adie SG, Marjanovic M, Chaney EJ, South FA, Monroy GL, et al. Intraoperative optical coherence tomography for assessing human lymph nodes for metastatic cancer. BMC Cancer [Internet]. 2016;16:144.

[33] El Beltagy MA, Aggag M, Kamal M. Role of intraoperative ultrasound in resection of pediatric brain tumors. Child's Nervous System. 2010;26:1189–93.

[34] Ivanovic NS, Zdravkovic DD, Skuric Z, Kostic J, Colakovic N, Stojiljkovic M, et al. Optimization of breast cancer excision by intraoperative ultrasound and marking needle - technique description and feasibility. World Journal of Surgical Oncology. BioMed Central; 2015;13:153.

[35] Veeratterapillay R, Bromby A, Patel A, Sakthivel A, Abdelbakhy A, Gowda BD, et al. Intraoperative and surgical specimen (ex vivo) ultrasound in the assessment of margins at partial nephrectomy. International Urology and Nephrology. 2015;47:1665–9.

[36] Moore MM, Whitney LA, Cerilli L, Imbrie JZ, Bunch M, Simpson VB, et al. Intraoperative ultrasound is associated with clear lumpectomy margins for palpable infiltrating ductal breast cancer. Annals of surgery. Lippincott, Williams, and Wilkins; 2001;233:761.

[37] Providian Medical Equipment. Ultrasound machines [Internet]. [cited 2017 Aug 13]. Available from: http://www.providianmedical.com/ultrasound-machine-application/intraoperative-procedures/

[38] Schäfer K-C, Dénes J, Albrecht K, Szaniszló T, Balog J, Skoumal R, et al. In Vivo, In Situ Tissue Analysis Using Rapid Evaporative Ionization Mass Spectrometry. Angewandte Chemie International Edition. 2009;48:8240–2.

[39] Balog J, Szaniszló T, Schaefer K-C, Denes J, Lopata A, Godorhazy L, et al. Identification of biological tissues by rapid evaporative ionization mass spectrometry. Analytical chemistry. 2010;82:7343–50.

[40] Waters Corporation. Price quote: REIMS Research System with iKnife Sampling Device. 2016.

[41] Baggish MS, Valle RF, Guedj H. Hysteroscopy: Visual perspectives of uterine anatomy, physiology and pathology. Lippincott Williams & Wilkins; 2007.

[42] Feldman LS, Fuchshuber PR, Jones DB. The SAGES Manual on the Fundamental Use of Surgical Energy (FUSE). Springer-Verlag New York. 2012.

[43] Arregui ME, Robert Jr J, Katkhouda N, McKernan JB, Reich H, others. Principles of laparoscopic surgery: basic and advanced techniques. Springer Science & Business Media; 2012.

[44] Capizzi PJ, Clay RP, Battey MJ. Microbiologic activity in laser resurfacing plume and debris. Lasers in Surgery and Medicine. 1998;23:172–4.

[45] Mowbray N, Ansell J, Warren N, Wall P, Torkington J. Is surgical smoke harmful to theater staff? a systematic review. Surgical Endoscopy and Other Interventional Techniques. 2013;27:3100–7.

[46] Tsuda A, Henry FS, Butler JP. Particle transport and deposition: basic physics of particle kinetics. Comprehensive Physiology. 2013;3(4):1437-1471.

[47] Thomas D, Charvet A, Bardin-Monnier N, Appert-Collin JC. Aerosol Filtration. Elsevier Science; 2016.

[48] NIOSH [2013]. Current strategies for engineering controls in nanomaterial production and downstream handling processes. Cincinnati, OH: U.S. DHHS (NIOSH) Publication No. 2014–102. :14–7.

[49] Hinds WC. Aerosol technology: properties, behavior, and measurement of airborne particles. John Wiley & Sons; 2012.

[50] Wilson AD, Baietto M. Applications and advances in electronic-nose technologies. Sensors. Molecular Diversity Preservation International; 2009;9:5099–148.

[51] Roine A, Saviauk T, Kumpulainen P, Karjalainen M, Tuokko A, Aittoniemi J, et al. Rapid and accurate detection of urinary pathogens by mobile IMS-based electronic nose: a proof-of-principle study. PloS one. Public Library of Science; 2014;9:e114279.

[52] Roine A, Veskimäe E, Tuokko A, Kumpulainen P, Koskimäki J, Keinänen TA, et al. Detection of prostate cancer by an electronic nose: a proof of principle study. The Journal of urology. Elsevier; 2014;192:230–5.

[53] Eiceman GA, Karpas Z, Hill Jr HH. Ion mobility spectrometry. CRC press; 2013.

[54] Cumeras R, Figueras E, Davis CE, Baumbach JI, Gràcia I. Review on Ion Mobility Spectrometry. Part 1: current instrumentation. The Analyst. 2015;140:1376–90.

[55] Buryakov IA, Krylov E V, Nazarov EG, Rasulev UK. A new method of separation of multi-atomic ions by mobility at atmospheric pressure using a high-frequency amplitude-asymmetric strong electric field. International Journal of Mass Spectrometry and Ion Processes. Elsevier; 1993;128:143–8.

[56] Schneider BB, Nazarov EG, Londry F, Vouros P, Covey TR. Differential mobility spectrometry/mass spectrometry history, theory, design optimization, simulations, and applications. Mass spectrometry reviews. Wiley Online Library; 2016;35:687–737.

[57] Krylov E V, Nazarov EG. Electric field dependence of the ion mobility. International Journal of Mass Spectrometry. Elsevier; 2009;285:149–56.

[58] Dove A. Mass Spectrometry for the Masses. Science. 2008;1115:1115–7.

[59] CBRNE Tech Index. Spectrometry [Internet]. [cited 2017 Jun 27]. Available from: http://www.cbrnetechindex.com/Chemical-Detection/Technology-CD/Spectrometry-CD-T

[60] Watson JT, Sparkman OD. Introduction to mass spectrometry: instrumentation, applications, and strategies for data interpretation. John Wiley & Sons; 2007.

[61] Shvartsburg AA, Seim TA, Danielson WF, Norheim R, Moore RJ, Anderson GA, et al. High-definition differential ion mobility spectrometry with resolving power up to 500. Journal of the American Society for Mass Spectrometry. Springer; 2013;24:109–14.

[62] MacCoun R, Perlmutter S. Hide results to seek the truth: more fields should, like particle physics, adopt blind analysis to thwart bias. Nature. Nature Publishing Group; 2015;526:187–90.

[63] Sammut C, Webb GI, editors. Supervised Learning. Encyclopedia of Machine Learning. Boston, MA: Springer US; 2010. p. 941.

[64] Periklis A, Panayiotis T. Categorical data clustering. In: Sammut C, Webb GI, editors. Encyclopedia of Machine Learning. Boston, MA: Springer US; 2010. p. 156.

[65] Kohonen T. Self-organized formation of topologically correct feature maps. Biological cybernetics. Springer; 1982;43:59–69.

[66] Wilkinson L, Friendly M. The history of the cluster heat map. The American Statistician. Taylor & Francis; 2009;63:179–84.

[67] Quadrianto N, Buntine WL. Linear Discriminant. In: Sammut C, Webb GI, editors. Encyclopedia of Machine Learning. Boston, MA: Springer US; 2010. p. 601–3.

[68] Vlachos M. Dimensionality Reduction. In: Sammut C, Webb GI, editors. Encyclopedia of Machine Learning. Boston, MA: Springer US; 2010. p. 274–9.

[69] Schäfer KC, Balog J, Szaniszló T, Szalay D, Mezey G, Dénes J, et al. Real time analysis of brain tissue by direct combination of ultrasonic surgical aspiration and sonic spray mass spectrometry. Analytical Chemistry. 2011;83:7729–35.

[70] Peterson LE. K-nearest neighbor. Scholarpedia. 2009;4:1883.

[71] Zhu X. Semi-Supervised Learning. In: Sammut C, Webb GI, editors. Encyclopedia of Machine Learning. Boston, MA: Springer US; 2010. p. 892–7.

[72] Webb GI. Overfitting. In: Sammut C, Webb GI, editors. Encyclopedia of Machine Learning. Boston, MA: Springer US; 2010. p. 744.

[73] Harrell Jr. FE, Lee KL, Mark DB. Multivariable prognostic models: Issues in developing models, evaluating assumptions and adequacy, and measuring and reducing errors. Statistics in Medicine. 1996;15:361–87.

[74] Sammut C, Webb GI, editors. Cross-validation. Encyclopedia of Machine Learning. Boston, MA: Springer US; 2010. p. 249.

[75] Steyerberg EW, Harrell FE. Prediction models need appropriate internal, internal--external, and external validation. Journal of clinical epidemiology. Elsevier; 2016;69:245–7.

[76] Sammut C, Webb GI, editors. Leave-One-Out Cross-Validation. Encyclopedia of Machine Learning. Boston, MA: Springer US; 2010. p. 600.

[77] Sammut C, Webb GI, editors. Artificial Neural Networks. Encyclopedia of Machine Learning. Boston, MA: Springer US; 2010. p. 44.

[78] Schmidhuber J. Deep Learning. In: Sammut C, Webb GI, editors. Encyclopedia of Machine Learning and Data Mining. Boston, MA: Springer US; 2017. p. 338–48.

[79] Parikh R, Mathai A, Parikh S, Sekhar GC, Thomas R. Understanding and using sensitivity, specificity and predictive values. Indian journal of ophthalmology. Medknow Publications; 2008;56:45.

[80] Currie LA. Nomenclature in evaluation of analytical methods including detection and quantification capabilities. Pure and Applied Chemistry. 1995;67:1699–723.

[81] Ting KM. Confusion Matrix. In: Sammut C, Webb GI, editors. Encyclopedia of Machine Learning. Boston, MA: Springer US; 2010. p. 209.

[82] Innokas Medical Oy. Itkacut 350MB datasheet. 2002.

[83] Laine T, Silenius M. Bachelor's thesis: Modified 3D-printer as an automated brain tissue sampler. Tampere University of Technology; 2015.

[84] Xu XW, Newman ST. Making CNC machine tools more open, interoperable and intelligent - A review of the technologies. Computers in Industry. 2006;57:141–52.

[85] Oksala N, Saari S, Karjalainen M, Kontunen A, Roine A. Method and apparatus for analyzing biological samples, Patent number: 20175319. Finland; 2017.

[86] Chen J, Davidson JH. Ozone production in the positive DC corona discharge: Model and comparison to experiments. Plasma chemistry and plasma processing. Springer; 2002;22:495–522.

[87] Leusink J. How does ozone kill bacteria? [Internet]. Ozone Solutions. OZONE Journal. 2010 [cited 2017 Aug 14]. Available from: http://www.ozonesolutions.com/journal/2010/how-does-ozone-kill-bacteria/

[88] Kowalski WJ, Bahnfleth WP, Whittam TS. Bactericidal effects of high airborne ozone concentrations on Escherichia coli and Staphylococcus aureus. Taylor & Francis; 1998;

[89] Yehia A, Mizuno A. Suppression of the ozone generation in the positive and negative dc corona discharges. International Journal of Plasma Environmental Science and Technology. 2008;2:44–9.

[90] Environics Oy. ENVI-AMC technical datasheet [Internet]. [cited 2017 Jun 14]. Available from: http://www.environics.fi/wp-content/uploads/2014/04/ENVI_AMC_real-time_AMC_monitoring_for_semiconductor_industry.pdf

[91] Ierusalimschy R. Programming in Lua. Roberto Ierusalimschy. 2006.

[92] Karjalainen M, Kontunen A, Saari S, Rönkkö T, Lekkala J, Roine A, et al. The Characterization of Surgical Smoke From Various Tissues and Its Implications for Occupational Safety. Manuscript submitted for publication. 2017.

[93] Keskinen J, Pietarinen K, Lehtimäki M. Electrical low pressure impactor. Journal of Aerosol Science. 1992;23:353–60.

[94] Järvinen A, Aitomaa M, Rostedt A, Keskinen J, Yli-Ojanperä J. Calibration of the new electrical low pressure impactor (ELPI+). Journal of Aerosol Science. 2014;69:150–9.

[95] Sullivan TP, Eaglstein WH, Davis SC, Mertz P. THE PIG AS A MODEL FOR HUMAN WOUND HEALING. Wound Repair and Regeneration. Blackwell Science Inc; 2001;9:66–76.

[96] Meurens F, Summerfield A, Nauwynck H, Saif L, Gerdts V. The pig: a model for human infectious diseases. Trends in microbiology. Elsevier; 2012;20:50–7.

[97] Jacobi U, Kaiser M, Toll R, Mangelsdorf S, Audring H, Otberg N, et al. Porcine ear skin: an in vitro model for human skin. Skin Research and Technology. Wiley Online Library; 2007;13:19–24.

[98] Milo R, Phillips R. Cell biology by the numbers [Internet]. [cited 2017 Jul 7]. Available from: http://book.bionumbers.org/how-big-are-viruses/